DEPARTMENT OF PHYSICS
UNIVERSITY OF JYVÄSKYLÄ
RESEARCH REPORT No. 4/2011

EVENT-BY-EVENT HYDRODYNAMICS AND THERMAL PHOTON PRODUCTION IN ULTRARELATIVISTIC HEAVY ION COLLISIONS

BY
HANNU HOLOPAINEN

Academic Dissertation
for the Degree of
Doctor of Philosophy

To be presented, by permission of the
Faculty of Mathematics and Natural Sciences
of the University of Jyväskylä,
for public examination in Auditorium FYS1 of the
University of Jyväskylä on September 16th, 2011
at 12 o'clock noon

Jyväskylä, Finland
August 2011

Preface

The work presented in this thesis was carried out at the Department of Physics of the University of Jyväskylä during the years 2008-2011.

First of all, I would like thank my supervisor Prof. Kari J. Eskola for the excellent guidance over these years. This work has not been done only by myself, and thus I want to express my gratitude to my collaborators Dr. Thorsten Renk, Dr. Sami Räsänen, Dr. Harri Niemi, Dr. Rupa Chatterjee, Mr. Jussi Auvinen and Mr. Risto Paatelainen from the University of Jyväskylä and Prof. Ulrich Heinz and Mr. Chun Shen from the Ohio State University. It has been a pleasure to work with you. I also want to thank Prof. Keijo Kajantie and Doc. Aleksi Vuorinen for reviewing the manuscript of this thesis and Assist. Prof. Derek Teaney for promising to be my opponent. In addition I would like to thank all my friends at the University of Jyväskylä for the enjoyable company. Last, but not least, I want to thank my parents and my wife Pinja for love and support.

The financial support from the Graduate School of Particle and Nuclear Physics (GRASPANP), the Rector of the University of Jyväskylä, the Academy of Finland and the Helsinki Institute of Physics (HIP) is gratefully acknowledged. The CSC IT Center for Science in Espoo, Finland, is acknowledged for the allocation of computational resources.

In addition, my visits to *Quark Matter 2009*, Knoxville, USA; *Quantifying the Properties of Hot QCD Matter* program, Seattle, USA; *Hard Probes 2010*, Eilat, Israel and *Quark Matter 2011*, Annecy, France, were supported by the Magnus Ehrnrooth Foundation at the Finnish Society of Sciences and Letters, the Vilho, Yrjö and Kalle Väisälä fund at the Finnish Academy of Science and Letters and the (U. S. Department of Energy's) Institute for Nuclear Theory at the University of Washington

Author Hannu Holopainen
Department of Physics
University of Jyväskylä
Finland

Supervisor Prof. Kari J. Eskola
Department of Physics
University of Jyväskylä
Finland

Reviewers Prof. Keijo Kajantie
Helsinki Institute of Physics
Finland

Doc. Aleksi Vuorinen
Faculty of Physics
Bielefeld University
Germany

Opponent Assist. Prof. Derek Teaney
Department of Physics & Astronomy
Stony Brook University
USA

List of publications

This thesis consists of an introductory part and the following publications:

I **Event-by-event hydrodynamics and elliptic flow from fluctuating initial state**, H. Holopainen, H. Niemi, K. J. Eskola, Phys. Rev. **C83** (2011) 034901, arXiv:1007.0368 [hep-ph].

II **A Systematic comparison of jet quenching in different fluid-dynamical models**, T. Renk, H. Holopainen, U. Heinz, C. Shen, Phys. Rev. **C83** (2011) 014910, arXiv:1010.1635 [hep-ph].

III **Enhancement of thermal photon production in event-by-event hydrodynamics**, R. Chatterjee, H. Holopainen, T. Renk, K. J. Eskola, Phys. Rev. **C83** (2011) 054908, arXiv:1102.4706 [hep-ph].

IV **Systematics of the charged-hadron P_T spectrum and the nuclear suppression factor in heavy-ion collisions from $\sqrt{s} = 200$ GeV to $\sqrt{s} = 2.76$ TeV**, T. Renk, H. Holopainen, R. Paatelainen, K. J. Eskola, accepted for publication in Phys. Rev. **C**, arXiv:1103.5308 [hep-ph].

V **Elliptic flow of thermal photons in heavy-ion collisions at Relativistic Heavy Ion Collider and Large Hadron Collider**, H. Holopainen, S. S. Räsänen, K. J. Eskola, submitted to Phys. Rev. **C**, arXiv:1104.5371 [hep-ph].

The author has developed the event-by-event hydrodynamical code which is used in publications [I-V]. Every part of the code, except the Cooper-Frye calculation and resonance decays, was written from the scratch. The author has done all the hydrodynamical calculations in articles [I,IV,V] and the "2+1d ideal" hydrodynamic calculations in [II]. The author has also written a code for thermal photon production and performed the photon calculations in [V] and done systematic cross checks for [III]. The draft versions of papers [I,V] were written by the author.

Contents

Chapter 1

Introduction

Quantum Chromodynamics (QCD) is a quantum field theory which describes the fundamental strong interactions. The elementary particles of this theory are quarks and gluons and they carry a color charge. In the nature the quarks and gluons are observed only through color neutral bound states called hadrons. Hundreds of these bound states have been measured in the experiments [1].

Already in the early years of QCD, the existence of a new phase, where quarks and gluons can move freely, was predicted, see e.g. Refs. [2, 3]. The most recent lattice QCD calculations have shown that at zero net-baryon chemical potential the hadronic matter transforms into this new phase at a temperature $T_c \sim 155$ MeV [4, 5]. Such hot and dense QCD matter, where partons are not bound to color neutral states, is called quark-gluon plasma (QGP).

The main goal of ultrarelativistic heavy-ion collisions (URHIC) is to produce and study the QGP. The four experiments at the Relativistic Heavy Ion Collider (RHIC) at BNL discovered that hot and dense QCD matter, which behaves as a nearly ideal fluid, is indeed formed in URHIC [6–9]. In these Au+Au collisions at $\sqrt{s_{NN}} = 200$ GeV the produced QGP starts to expand very rapidly and it quickly cools down and the transition back to the hadronic matter takes place. Since the lifetime of the produced QGP is very short and only the final state hadrons, as well as some electromagnetic signatures, are measurable, it is very challenging to measure the plasma properties.

In these nucleus+nucleus ($A + A$) collisions, most of the observed bulk matter is initially produced through non-perturbative processes where perturbative QCD (pQCD) cannot be utilized as straightforwardly as in high-p_T physics in proton+proton (p+p) collisions. Neither the lattice approach works in the rapidly expanding system. Thus, alternative ways are needed to describe the dynamics of the URHIC. Since $\mathcal{O}(1000)$ partons are produced at the mid-rapidity unit in the heavy-ion experiments at RHIC and the Large Hadron Collider (LHC) at CERN, one can try to develop models based on statistical mechanics.

One possibility is to study these collisions with a microscopic approach [10–13]. In this case the matter is described using quarks and gluons and their interactions. These kind of models are usually called parton cascades. The interactions between quarks and gluons are usually well understood only in the pQCD framework, which may not be applicable in the cascade's thermal scale processes. In addition, the phase transition from partons to hadrons is not yet understood at the microscopical level.

Another possibility is to model the produced QGP with relativistic hydrodynamics [14–20]. In the hydrodynamical models the matter is treated as a continuous fluid which is at local equilibrium or at least close to it. In this case the dynamical properties of the medium are given by the Equation of State (EoS). The expansion of the system is obtained from the differential equations which by construction conserve energy and momentum. This approach is much simpler than the microscopic ones and another major advantage is that in this case there is no need to know the microscopical details of the phase transition or even the degrees of freedom, which are automatically encoded in the EoS.

The main inputs to the hydrodynamical calculations are the EoS and the initial state. The EoS at zero baryochemical potential (good approximation for RHIC and LHC) can be extracted from the lattice calculations [21, 22], but the initial state is much more difficult to obtain. There are models such as the EKRT [23] and the color glass condensate (CGC) approaches [24–26] for computing the primary parton production, but thermalization is not understood in any of these models. If dissipative effects are taken into account, one also needs the transports coefficients of the fluid (e.g. shear viscosity). Since these coefficients for QCD are not yet fully known, one can try to constrain them, as well as the initial state, using the experimental data [27–31].

One of the most important experimental observables from the hydrodynamical viewpoint is the elliptic flow, v_2, which measures the azimuthal anisotropy of the final state particle distributions. A large elliptic flow has been considered as a sign of hydrodynamical pressure: If $A+A$ collisions would be mere superpositions of nucleon+nucleon collisions, the final particle distributions should be nearly isotropic in the transverse plane. If a thermalized medium is formed in such collisions, the particle production has preferred directions due to the initial state geometry.

Another great discovery of the RHIC heavy-ion experiments was the high-p_T hadron suppression [32, 33], so called jet-quenching. Since the high-energy partons must traverse through the formed medium, they interact with it and lose energy. Thus understanding the high-p_T data in $A + A$ collisions also requires input from the low-p_T part described by hydrodynamics.

Unlike partons, photons can escape from the medium without interacting since the electromagnetic coupling is much weaker than the strong one. Thus the photons have a great potential to probe the medium at the time they were produced.

These two examples show that the medium can be studied not only looking at the small-p_T hadron production, but also considering other probes.

In this thesis the effects of initial state density fluctuations are studied using ideal event-by-event hydrodynamics and the main focus is on the elliptic flow of hadrons at RHIC. Also the transverse momentum spectra of thermal photons are studied with the initial state fluctuations. In addition, the elliptic flow of photons is considered for RHIC and LHC, but in these studies the initial state fluctuations are neglected for simplicity. Finally the suppression of high-energy hadrons is discussed briefly from the viewpoint of hydrodynamics.

This thesis consists of five original papers [I, II, III, IV, V] and an introductory part presented below. The hydrodynamical model is introduced in Chapter 2. The initial state modeling is presented in Chapter 3 and the hydrodynamical flow analysis methods are discussed in Chapter 4. In Chapter 5 the thermal photons and hard partons are considered as probes for the QGP matter. The obtained main results are summarized in Chapter 6 and finally the conclusions and outlook are given in Chapter 7.

Chapter 2

Hydrodynamical modeling

In hydrodynamics the system of interest is described with a few macroscopic variables like pressure and shear viscosity. If the parameters of the underlying microscopic system are known, the hydrodynamical calculations are relatively easy to perform. This simplicity is one of the main advantages of the hydrodynamical models over the microscopical ones, where the interactions of the particles must be modeled in a detailed manner. Another major advantage is that the phase transition from the QCD plasma to the hadron gas is conveniently taken into account through the EoS.

However, the hydrodynamical models need crucial external input. Hydrodynamics itself cannot tell anything about the initial state, EoS or transport coefficients. The EoS is quite well constrained at the zero net-baryon chemical potential by the lattice QCD calculations, but the initial state and transport coefficients are theoretically more badly known. Experimental data from RHIC and LHC, however, can give constraints for these unknowns. For example the current estimates show that the shear viscosity, η, is small [27–31].

Hydrodynamics assumes that matter is close to thermodynamical equilibrium but currently it is not understood how the system formed in URHIC actually thermalizes. This obviously causes problems since it is not known precisely when the assumption of thermal equilibrium is fulfilled and thus it is not clear when the hydrodynamical evolution can be started.

In this Chapter I will introduce the ideal hydrodynamical equations in the longitudinally boost-invariant case and discuss the EoSs which we apply. In addition, further modeling, which is needed to convert the hydrodynamical state to measurable final state particles in our framework, will be discussed. I also briefly comment on the dissipative effects, although they are not included in the calculations shown here. The discussion of the initial states is presented separately in Chapter 3.

2.1 Ideal hydrodynamics

In hydrodynamics the conservation equations are solved for the energy-momentum tensor $T^{\mu\nu}(x)$ and conserved currents $N_i^\mu(x)$:

$$\begin{aligned} \partial_\mu T^{\mu\nu} &= 0 \\ \partial_\mu N_i^\mu &= 0. \end{aligned} \tag{2.1}$$

Usually the only conserved current that is taken into account is the net-baryon number current. In this thesis the focus is on mid-rapidities in Au+Au collisions at $\sqrt{s_{NN}} = 200$ GeV and Pb+Pb collisions at $\sqrt{s_{NN}} = 2.76$ TeV, and therefore the net-baryon number can be assumed to be negligible at all times. However, at lower energies (e.g at CERN-SPS) the net-baryon number must be considered.

In the general case $T^{\mu\nu}(x)$ has 10 unknown components, since it must be symmetric. The Eq. (2.1) gives, however, only 4 independent equations for $T^{\mu\nu}$. Thus the set of equations is not closed; the number of variables must be reduced and one needs to provide more equations. In the ideal hydrodynamic case, where the local thermal equilibrium is assumed, $T^{\mu\nu}(x)$ can be decomposed as [34]

$$T^{\mu\nu} = \epsilon u^\mu u^\nu - P\Delta^{\mu\nu}, \tag{2.2}$$

where $\epsilon(x)$ is the energy density, P is the pressure, u^μ is the fluid four-velocity, and

$$\Delta^{\mu\nu} = g^{\mu\nu} - u^\mu u^\nu \tag{2.3}$$

is a projection operator, which picks the components orthogonal to u^μ. In this case there are only 5 independent variables (ϵ, P and 3 components of u^μ). To obtain a closed set of equations, an EoS $P = P(\epsilon)$ must be introduced.

2.2 2+1 dimensional case

Hydrodynamical calculations presented in this thesis assume longitudinal boost-invariance [14] and thus the numerical problem is only 2+1-dimensional. This assumption has been a standard approach to hydrodynamics in the recent years. However, also a number of full 3+1-dimensional codes exists [35–38].

It is convenient to use the proper time τ and spacetime rapidity η_s to describe the system coordinates instead of time t and longitudinal coordinate z. They are defined as

$$\tau = \sqrt{t^2 - z^2} \qquad \eta_s = \frac{1}{2}\ln\frac{t+z}{t-z}. \tag{2.4}$$

Now in the boost invariant case the flow velocity is

$$u^\mu = \gamma_T(\cosh\eta_s, v_x, v_x, \sinh\eta_s), \tag{2.5}$$

where $\gamma_T = 1/\sqrt{1-v_x^2-v_y^2}$ is the Lorentz gamma factor for the transverse components. This means that the velocity in the direction of the z-axis is assumed to be $v_z = z/t$. Thus the expansion is really 3+1 dimensional, but the expansion in the z-direction is trivial. Another way to say this is that the system looks similar at every rapidity at a constant proper time.

This approximation is valid in the mid-rapidity, since the measured dN/dy distributions are approximately flat in this region [39]. Obviously this simplification breaks down when forward or backward rapidities are considered and there one must numerically solve the full 3+1-dimensional problem. For this reason only mid-rapidity particle production can be considered in this thesis.

With these assumptions the hydrodynamical equations can be written as

$$\begin{aligned}
\partial_\tau T^{\tau\tau} &= -\partial_x(w_x T^{\tau\tau}) - \partial_y(w_y T^{\tau\tau}) - \frac{1}{\tau}(T^{\tau\tau} + P) \\
\partial_\tau T^{\tau x} &= -\partial_x(v_x T^{\tau x}) - \partial_y(v_y T^{\tau x}) - \frac{1}{\tau} T^{\tau x} - \partial_x P \\
\partial_\tau T^{\tau y} &= -\partial_x(v_x T^{\tau y}) - \partial_y(v_y T^{\tau y}) - \frac{1}{\tau} T^{\tau y} - \partial_y P,
\end{aligned} \tag{2.6}$$

where $w_i = T^{\tau i}/T^{\tau\tau}$ is a speed-like quantity. These equations are solved numerically using the SHArp and Smooth Transport Algorithm (SHASTA) [40, 41]. This algorithm can handle shockwaves that are produced for example when one uses an EoS with a first order phase transition. Also the initial states with density fluctuations may cause shockwaves. The details of how the algorithm is implemented can be found in Ref. [42].

After each timestep taken with the SHASTA algorithm, the energy-momentum tensor components have updated values. The energy density and velocities still need to be solved. First the energy density is obtained from

$$\epsilon = T^{\tau\tau} - \sum_{i=x,y} \frac{(T^{\tau i})^2}{T^{\tau\tau} + P(\epsilon)}. \tag{2.7}$$

Since in general the EoS is a complicated function of ϵ, this equation must be solved with some iterative method. When the energy density is known, the flow velocities are given by

$$v^i = \frac{T^{\tau i}}{T^{\tau\tau} + P(\epsilon)}. \tag{2.8}$$

After this the next timestep can be taken with the SHASTA.

2.3 Equation of state

The EoS is one of the key inputs to the hydrodynamical calculations. In principle one of the goals in the heavy-ion physics is to get information about the

EoS. In practice this has turned out to be very difficult since the hydrodynamical calculations (observables) are quite insensitive to the EoS [21].

In this thesis three different EoSs are used. One of them is a bag model EoS (eosQ) [43]. At high temperatures the eosQ is constructed from the ideal gas of massless quarks and gluons with a bag constant. An ideal hadron resonance gas (HG), where all hadrons with mass $m < 2$ GeV are taken into account, is assumed in the low temperature phase. These two phases are connected with a mixed phase and the bag constant is fixed so that the first-order phase transition takes place at $T_c = 165$ MeV.

The other two EoSs have a cross-over phase transition. The s95p [21] is an EoS extracted from the lattice data and the eosL from Ref. [44] is based on an effective theory calculation. Both of these EoSs are matched to the HG at the low temperatures.

In Fig. 2.1 I have plotted the energy density as a function of temperature. The eosQ, which has the first order phase transition, clearly separates from the cross-over EoSs at the phase transition temperature. From a hydrodynamical point of view the most crucial difference between these cases is that in the mixed phase of the eosQ the pressure is constant and thus no flow is generated there. In the

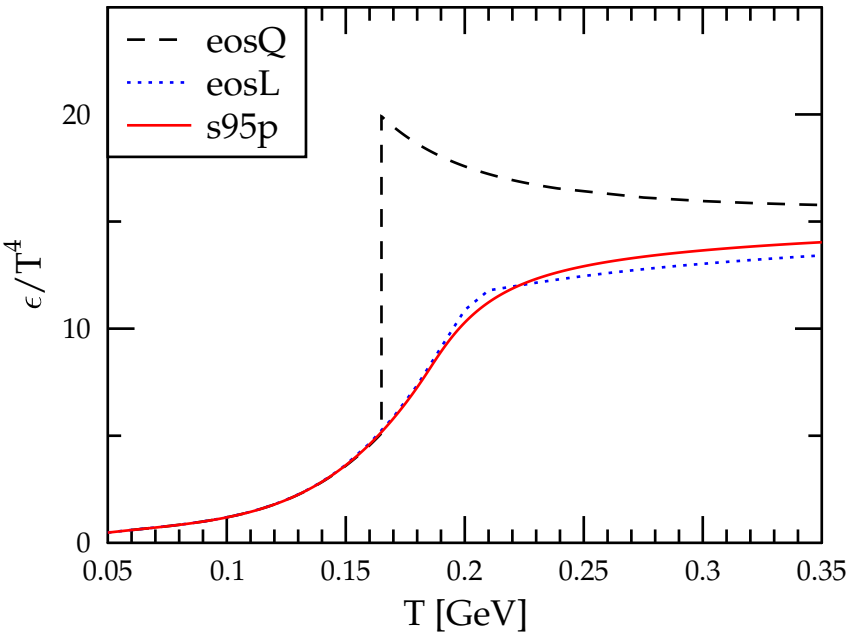

Figure 2.1: The energy density, scaled with the appropriate power of temperature, as a function of temperature for the three EoSs considered in this thesis.

cross-over phase transition EoSs the pressure gradients are always present and thus the flow can develop at all times.

2.4 Freeze-out

Once the hydrodynamical evolution is at the end, the observable final-state particles must be generated from the fluid elements. A common way to handle this is to define a hyper-surface, where the freeze-out happens instantly, and assume that the hadrons which are outside this 4-volume are free particles. Usually one uses the following Cooper-Frye method to calculate the particle emission from the freeze-out surface [45].

The hyper-surface is determined by posing some freeze-out condition. A commonly used criterion is to assume that the freeze-out happens at a constant temperature. Also more dynamical freeze-out conditions can be developed as was shown in Ref. [46], where the local expansion rate was compared to the local scattering rate of the particles. However, all hadron species do not necessary decouple at the same time since the interaction cross sections are different. Thus in some hydrodynamical models [37, 47–53] the "freeze-out" is done when the hadrons still interact and the produced particles are fed into a hadron cascade.

In this thesis a constant-temperature freeze-out surface Σ is assumed and the transverse momentum spectrum for a hadron type i is calculated from [45]

$$\frac{dN_i}{d^2p_T dY} = \int_\Sigma f_i(x,p) p^\mu d\Sigma_\mu, \tag{2.9}$$

where $d\Sigma_\mu$ is a surface element and $f_i(x,p)$ is the momentum distribution function for the particle species i. Since boost-invariance is assumed, the surface can be parameterized as

$$\Sigma^\mu = (\tau(x,y)\cosh\eta_s, x, y, \tau(x,y)\sinh\eta_s) \tag{2.10}$$

and the surface element is then [42, 54]

$$\begin{aligned} d\Sigma_\mu &= -[\pm]\epsilon_{\mu\nu\lambda\rho}\frac{\partial\Sigma^\nu}{\partial x}\frac{\partial\Sigma^\lambda}{\partial y}\frac{\partial\Sigma^\rho}{\partial\eta_s}dxdyd\eta_s \\ &= [\pm](\cosh\eta_s, -\frac{\partial\tau}{\partial x}, -\frac{\partial\tau}{\partial y}, -\sinh\eta_s)\tau dxdyd\eta_s, \end{aligned} \tag{2.11}$$

where $\epsilon_{\mu\nu\lambda\rho}$ is the totally antisymmetric Levi-Civita symbol ($\epsilon^{\mu\nu\lambda\rho} = -\epsilon_{\mu\nu\lambda\rho}$ and $\epsilon^{0123} = +1$) and $[\pm]$ ensures that the surface normal vector points in the direction of the decreasing temperature. The outgoing particle has a momentum

$$p^\mu = (m_T\cosh Y, p_x, p_y, m_T\sinh Y), \tag{2.12}$$

where Y is the rapidity of the particle and $m_T = \sqrt{m^2 + p_T^2}$ is the transverse mass. Now everything can be inserted into Eq. (2.9) and if the momentum distribution function is written as a geometrical series,

$$\frac{1}{e^x \mp 1} = \frac{e^{-x}}{1 \mp e^{-x}} = e^{-x} \sum_{n=0}^{\infty} (\pm 1)^n e^{-nx}, \tag{2.13}$$

the η_s integral can be calculated analytically. Finally Eq. (2.9) can be expressed as [42]

$$\begin{aligned} \frac{dN_i}{d^2p_T dY} =& \frac{g}{(2\pi)^3} \sum_{n=1}^{\infty} (\pm 1)^{n+1} \int_{\Sigma} dxdy[\pm]\tau \exp\left[\frac{n\mu}{T} + \frac{n\gamma_T \boldsymbol{p_T} \cdot \boldsymbol{v_T}}{T}\right] \\ & \left[m_T K_1\Big(\frac{n\gamma_T m_T}{T}\Big) - \Big(\frac{\partial \tau}{\partial x} p_x + \frac{\partial \tau}{\partial y} p_y\Big) K_0\Big(\frac{n\gamma_T m_T}{T}\Big)\right], \end{aligned} \tag{2.14}$$

where g is the degeneracy factor for the hadron type i, and K_0 and K_1 are the modified Bessel functions of the second kind [55] coming from the η_s integration. The x- and y-integrations must then be done numerically. If the situation is azimuthally symmetric, also the polar angle integration can be done analytically.

2.5 Event-by-event framework

Traditionally the hydrodynamical calculations have been performed with smooth initial states, ignoring the initial density fluctuations. However, first calculations with bumpy initial states were introduced in the 90s [56] and in the last few years many event-by-event models for hydrodynamics have been developed [57–66, I]. Here I discuss the event-by-event framework introduced in Ref. [I].

In our case the initial states are taken from the Monte Carlo Glauber model as described in the next Chapter. For each event the hydrodynamical evolution and thermal spectra calculation are done as explained above. At these stages the fluctuating initial states are treated in the same way as the smooth ones. After the thermal spectra are obtained from each event, the hadrons are generated by sampling these distributions. First some wide enough rapidity interval is chosen and the total number of particles in this interval is calculated. Then the transverse momenta and azimuthal angles of hadrons are generated by using the thermal spectra as probability distributions. Since the longitudinal boost-invariance is assumed, the rapidity is taken randomly from a flat distribution. In this thesis a rapidity interval $|Y| < 0.5$ is used by default.

Since in the end the observables are obtained as an average over the produced events, a lot of events are needed in order to get results with reasonable statistical

errors. One hydrodynamical run and the calculation of thermal spectra takes about one hour of CPU time with a modern computer and thus one needs a lot of computational power to make 10 000 events. However one can capture the most interesting hydrodynamical properties already with a much smaller number of events. Since sampling of the thermal spectrum is much faster than making the hydrodynamical part, in here 20 events are sampled from each hydro run. Thus the statistics of 10 000 events are obtained with only 500 time-consuming hydro events.

2.6 Resonance decays

The HG phase in the EoSs used in this thesis has roughly 300 particle species. Most of these hadrons are heavy resonances, which decay through the strong and electromagnetic interactions. Due to their short lifetime, these hadrons cannot be directly measured at the experiments. Thus one must do the decays to be able to compare with the experimental data.

If the freeze-out is done at high enough temperatures, the contribution from the heavy resonance decays to pions, kaons and protons is significant [67]. Especially with the relatively high freeze-out temperatures used in this thesis, the decays are very important since most of the stable particles are coming from the resonance decays. How to do the decays in the case of smooth hydrodynamics (without sampling the thermal spectra) is presented in Refs. [42, 68, 69]. Below I will present how the decays can be done in the event-by-event framework, although in practice the decay routines from PYTHIA 6.4 [70] have been used to obtain the results in Ref. [I] and the event-by-event results presented in here.

Let us first consider the 2-particle decay ($a \to 1 + 2$) of a heavy resonance a with mass M. In this case the decay rate Γ in the rest frame of the decaying particle is

$$\begin{aligned}\Gamma_{1\to 2} =& \frac{g(M^2)}{2M}\int \frac{d^3\boldsymbol{p_1}}{2E_1}\frac{d^3\boldsymbol{p_2}}{2E_2}\delta^{(4)}(p_a - p_1 - p_2) \\ =& \frac{g(M^2)}{2M} I(M, m_1, m_2),\end{aligned} \tag{2.15}$$

where $g(M^2)$ is the squared matrix element, which is here taken to depend only on the mass of the decaying particle. Above I also defined

$$I(M, m_1, m_2) = \int \frac{d^3\boldsymbol{p_1}}{2E_1}\frac{d^3\boldsymbol{p_2}}{2E_2}\delta^{(4)}(p_a - p_1 - p_2), \tag{2.16}$$

which can be conveniently calculated in the rest frame of the decaying particle.

Since the energy and momentum are conserved, both particles 1 and 2 must have

$$|\boldsymbol{p_{1,2}}| = \frac{\sqrt{\lambda(M^2, m_1^2, m_2^2)}}{2M}, \tag{2.17}$$

where

$$\lambda(x, y, z) = x^2 + y^2 + z^2 - 2xy - 2xz - 2yz. \tag{2.18}$$

Integrals in Eq. (2.16) can now be solved and the result is

$$I(M, m_1, m_2) = \frac{\pi}{2M^2}\sqrt{\lambda(M^2, m_1^2, m_2^2)}. \tag{2.19}$$

Thus the final result for the decay width in the rest frame of the decaying particle is

$$\Gamma_{1\to 2} = \frac{\pi g(M^2)}{4M^3}\sqrt{\lambda(M^2, m_1^2, m_2^2)}. \tag{2.20}$$

In practice one first randomly chooses which decay channel is considered according to the branching ratios. Then the boost to the rest frame of the decaying particle is made and the momentum for decay products is calculated from Eq. (2.17). The direction of the particle 1 is taken randomly and the direction of the particle 2 is fixed by momentum conservation. Then the boosts back to the original frame are made.

Let us then consider the 3-particle decays. In this case the decay rate is

$$\Gamma_{1\to 3} = \frac{g(M^2)}{2E}\int \frac{d^3\boldsymbol{p_1}}{2E_1}\frac{d^3\boldsymbol{p_2}}{2E_2}\frac{d^3\boldsymbol{p_3}}{2E_3}\delta^{(4)}(p_a - p_1 - p_2 - p_3), \tag{2.21}$$

where again we assume for simplicity that the squared matrix element depends only on M. We may define

$$\boldsymbol{p_{23}} = \boldsymbol{p_2} + \boldsymbol{p_3} \qquad \boldsymbol{p} = \boldsymbol{p_2} - \boldsymbol{p_3} \tag{2.22}$$

where $\boldsymbol{p_{23}}$ is the momentum of the particle pair. The invariant mass of the pair, m_{23}, has the following limits

$$(m_2 + m_3)^2 \le m_{23}^2 \le (M - m_1)^2. \tag{2.23}$$

Since the phase phase element of the particle pair is invariant, it can be calculated in any frame. In the center of mass (CM) frame of the particle pair, one can write

$$\begin{aligned} m_{23}^2 &= (p_2 + p_3)^2 = (E_2 + E_3)^2 \\ &= \left(\sqrt{m_2^2 + (\boldsymbol{p}/2)^2} + \sqrt{m_3^2 + (-\boldsymbol{p}/2)^2}\right)^2 \end{aligned} \tag{2.24}$$

and from this one can solve

$$p = |\boldsymbol{p}| = \frac{\sqrt{\lambda(m_{23}^2, m_2^2, m_3^2)}}{m_{23}}. \tag{2.25}$$

Then the differentiation of Eq. (2.24) gives (in this frame $E_{23} = m_{23}$)

$$\frac{dm_{23}^2}{E_{23} m_{23}} = \frac{p\, dp}{2E_2 E_3} \tag{2.26}$$

and using the above definitions and results the phase space element becomes

$$\frac{d^3\boldsymbol{p_2}}{2E_2}\frac{d^3\boldsymbol{p_3}}{2E_3} = \frac{1}{2}\frac{d^3\boldsymbol{p_{23}} d^3\boldsymbol{p}}{4E_2 E_3} = \frac{2\pi\sqrt{\lambda(m_{23}^2, m_2^2, m_3^2)}}{m_{23}^2} dm_{23}^2 \frac{d^3\boldsymbol{p_{23}}}{2E_{23}}, \tag{2.27}$$

where the angular part of the $\boldsymbol{p}$ integral gives just 4π. Now all that is left in the 3-particle decay is the dm_{23}^2 integral and a part which is exactly similar to Eq. (2.16) which was calculated in the 2-particle decay. So finally in the rest frame of the decaying particle, we arrive at

$$\begin{aligned} \frac{d\Gamma_{1\to 3}}{dm_{23}^2} &= \frac{g(M^2)\pi}{M m_{23}^2}\sqrt{\lambda(m_{23}^2, m_2^2, m_3^2)} \int \frac{d^3\boldsymbol{p_1}}{2E_1}\frac{d^3\boldsymbol{p_{23}}}{2E_{23}}\delta^{(4)}(p_a - p_1 - p_{23}) \\ &= \frac{g(M^2)\pi^2}{2M^3 m_{23}^2}\sqrt{\lambda(M^2, m_1^2, m_{23}^2)}\sqrt{\lambda(m_{23}^2, m_2^2, m_3^2)}. \end{aligned} \tag{2.28}$$

Now in practice the invariant mass m_{23} must be sampled from the above distribution. After this the momentum for the particle 1 and particle pair is calculated from Eq. (2.17) by replacing m_2 with m_{23}. Again the direction of the particle 1 is taken randomly and momentum conservation fixes the angles of the particle pair. After this a boost to the rest frame of the particle pair is made and the "decay" from the particle pair to particles 2 and 3 is done as in the 2-particle case. Finally the decay products are boosted back into the original frame.

2.7 Dissipative effects

If the system is not exactly in thermal equilibrium, but close to it, hydrodynamics can still be used, but the dissipative effects must be taken into account. When the first-order velocity gradients are included, the energy-momentum tensor can be written as

$$T^{\mu\nu} = \epsilon u^\mu u^\nu - (P + \Pi)\Delta^{\mu\nu} + \pi^{\mu\nu} + W^\mu u^\nu + W^\nu u^\mu, \tag{2.29}$$

where Π is the bulk pressure, $\pi^{\mu\nu}$ is the shear stress tensor and W^μ is the heat flow. The net-baryon number current is

$$N^\mu = nu^\mu + V^\mu, \tag{2.30}$$

where V^μ is the diffusion current. In this case one must more carefully specify what the flow velocity is. There are two typical choices: the Eckart frame [71], where the flow is tied to net charge flow ($V^\mu = 0$), and the Landau frame [34], where the energy flow determines the flow velocity ($W^\mu = 0$).

However, these first-order Navier-Stokes equations are acausal (see e.g. Sec. IIB in Ref. [72]) and higher order terms must be considered. Israel and Stewart (IS) [73, 74] formulated the second-order dissipative hydrodynamics long time ago, but only recently these ideas have been adopted into the modeling of URHIC [75, 76]. In the IS formalism the dissipative quantities have their own evolution equations, which must be solved simultaneously with the Eqs. (2.1). In these equations new constants must be introduced and these must be obtained from elsewhere.

It has turned out that in the heavy-ion context the shear viscosity is the most important dissipative quantity and almost all calculations neglect the other dissipative corrections. The development of the viscous hydrodynamical frameworks has been very rapid in the recent years. The first 1+1-dimensional results were presented in Refs. [54, 77, 78] and soon after those many 2+1-dimensional hydrodynamical calculations have been published [27–31, 51–53, 79–84]. Very recently even a full 3+1-dimensional event-by-event viscous hydrodynamical framework was developed in Ref. [63]. All of the above calculations have included only the shear viscosity. The bulk viscosity effects have been studied for example in Refs. [85, 86].

When the dissipative effects are included, also the momentum distribution function $f(x, p)$ must have a correction δf arising from the non-equilibrium effects. Hydrodynamical simulations have shown that the viscous corrections to e.g. elliptic flow due to the δf term in the freeze-out calculation cannot be neglected [81, 87, 88]. Currently the exact form of the δf is, however, not known for the QCD matter, but for some other systems it has been calculated [87].

Chapter 3

Initial state

The initial state is a vitally important input for the hydrodynamical calculations. Since it is experimentally very difficult to study the initial state directly with e.g. electromagnetic probes, constraining the initial state is quite challenging: the initial state must be evolved to the measurable final state particles with a hydrodynamical model and the uncertainties related to the hydrodynamical description of the QCD matter are translated into uncertainties of the initial state.

In this thesis I assume longitudinal boost-invariance and hence the initial density profile is needed only in the transverse plane. Here the transverse profiles are obtained simply from different versions of the Glauber model (see e.g. [89]), where one considers only the collisions between nucleons. However, the Glauber model does not give the overall normalization of the densities. Thus the normalization must be fixed using the measured total multiplicity or some initial state model.

The initial proper time, τ_0, for hydrodynamics is rather difficult to constrain on the basis of the experimental data. Since the pressure gradients are large at the early times, the development of flow is sensitive to the initial time. However, since also the freeze-out temperature can be tuned, one can usually find a combination of τ_0 and T_f which produces the correct amount of flow. Consequently, in the hydrodynamical calculations at RHIC one uses a wide range of initial times $\tau_0 = 0.15 \ldots 1.0$ fm [27, 90].

In principle the thermal photon p_T-spectra are very sensitive to τ_0 [91, 92], but the initial time affects the p_T region, where also other photon production mechanisms can be important. Thus the uncertainties of τ_0 are so large that no firm conclusions about the initial time can be made currently based on the data alone. In Sec. 3.6 below, I will discuss how τ_0 can be obtained from the EKRT model.

3.1 Optical Glauber model

In the optical Glauber model it is assumed that a nucleon sees the other colliding nucleus as a smooth density distribution. The nuclear density ρ for the nucleus with a mass number A, according to standard two-parameter Woods-Saxon (W-S) potential, is

$$\rho(\boldsymbol{r}) = \frac{\rho_0}{1 + \exp[(|\boldsymbol{r}| - R_A)/d]}, \tag{3.1}$$

where R_A is radius of the nucleus, d is the surface thickness and ρ_0 is a normalization constant. The normalization is chosen so that

$$\int d^3\boldsymbol{r}\, \rho(\boldsymbol{r}) = A. \tag{3.2}$$

In the following only the transverse coordinates are considered and hence it is convenient to introduce the nuclear thickness function

$$T_A(x, y) = \int dz\, \rho(\boldsymbol{r}), \tag{3.3}$$

where the integration over the longitudinal direction is already made.

The two colliding nuclei, A and B, are separated by an impact parameter $\boldsymbol{b}$. Here it is assumed that the impact parameter is always pointing in the direction of the positive x-axis and the origin is located at the CM of the colliding nuclei as shown in Fig. 3.1. The impact parameter together with the z-axis define the reaction plane (RP).

In order to calculate the number of binary nucleon-nucleon collisions (BC), a small tube with an area $dxdy$ is considered. At this location the number of the collisions is given in terms of the nuclear thicknesses of A and B and the inelastic nucleon-nucleon cross section σ_{NN} as

$$dN_{\text{bin}} = \sigma_{NN} T_A(x + b/2, y) T_B(x - b/2, y)\, dxdy. \tag{3.4}$$

When the integration over the transverse plane is made, the total number of BC is

$$N_{\text{bin}} = \sigma_{NN} T_{AB}(b), \tag{3.5}$$

where the nuclear overlap function is defined as

$$T_{AB}(b) = \int dxdy\, T_A(x + b/2, y) T_B(x - b/2, y). \tag{3.6}$$

To obtain the number of participants, also called wounded nucleons (WN), one starts by considering the collision between one nucleon from A and a small tube from the nucleus B. The probability to have a collision with a nucleon from B is

$$P_{NB} = \frac{\sigma_{NN} T_B(x - b/2, y)}{B}. \tag{3.7}$$

From this, one gets the probability for the case that nucleon from A does not collide with any of the nucleons in the nucleus B

$$P = \Big(1 - \frac{\sigma_{NN} T_B(x - b/2, y)}{B}\Big)^B. \tag{3.8}$$

Thus the number of wounded nucleons in the nucleus A in the tube is

$$\begin{aligned} \frac{d^2 N^A_{\text{part}}}{dxdy} &= T_A(x + b/2, y)\Big[1 - \Big(1 - \frac{\sigma_{NN} T_B(x - b/2, y)}{B}\Big)^B\Big] \\ &\approx T_A(x + b/2, y)\Big[1 - \exp\Big(-\sigma_{NN} T_B(x - b/2, y)\Big)\Big], \end{aligned} \tag{3.9}$$

and finally the total number of wounded nucleons becomes

$$\begin{aligned} \frac{dN_{\text{part}}}{dxdy} &= T_A(x + b/2, y)\Big[1 - \exp\Big(-\sigma_{NN} T_B(x - b/2, y)\Big)\Big] \\ &+ T_B(x - b/2, y)\Big[1 - \exp\Big(-\sigma_{NN} T_A(x + b/2, y)\Big)\Big]. \end{aligned} \tag{3.10}$$

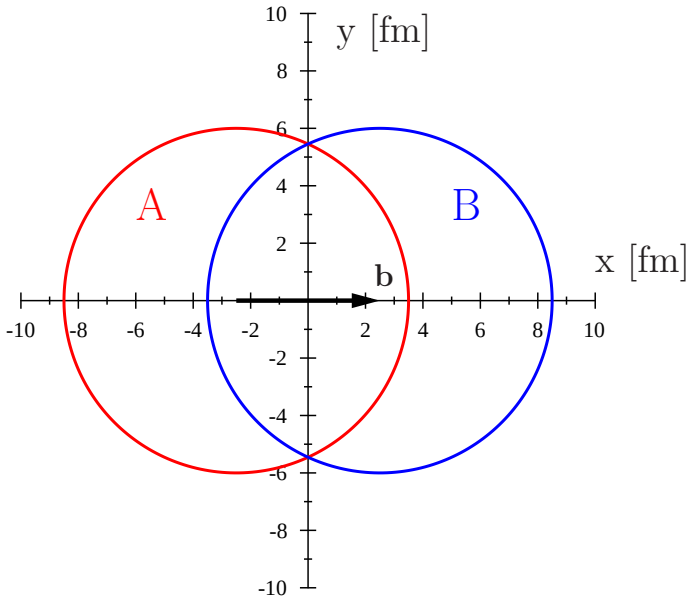

Figure 3.1: The colliding nuclei A and B separated by an impact parameter $\boldsymbol{b}$.

The binary collision and wounded nucleon distributions can be used to model the initial transverse profiles for the energy density (eBC, eWN) or for the entropy density (sBC, sWN) [93]:

$$\begin{aligned} \epsilon[s] &= K_{\mathrm{WN}} \frac{dN_{\mathrm{part}}}{dxdy} \\ \epsilon[s] &= K_{\mathrm{BC}} \frac{dN_{\mathrm{bin}}}{dxdy}, \end{aligned} \tag{3.11}$$

where K_{WN} and K_{BC} are overall (case-specific) normalization constants, which must be fixed by using some initial state model or the measured multiplicity. However, none of these initial states explains the data perfectly. A way to improve the initial state Glauber modeling is to use the centrality dependence of the charged hadron multiplicity and find a mix of BC and WN profiles which fits well with the data [94]. All of the optical Glauber initial states considered above are, however, smooth and no event-by-event density fluctuations are included in these cases.

3.2 Monte Carlo Glauber model

In the Monte Carlo Glauber (MCG) approach the initial density fluctuations are included in a natural way. Thus MCG is a convenient choice for the initial states of event-by-event hydrodynamics. In this approach one starts by generating random nuclear configurations using the W-S potential as a probability distribution. The W-S potential does not give any information about 2-nucleon correlations, and thus it is possible that two or more nucleons have a large overlap volume, which in principle is an unphysical phenomenon.

In the Ref. [95] more sophisticated nucleon configurations were obtained and tabulated configurations could be easily used to solve the problems with 2-nucleon correlations in this MCG model [96]. Another possibility is to simulate the finite size of nucleons by including an exclusion radius [97]. After a nucleon position is sampled from the W-S distribution one checks if there already exists a nucleon within the exclusion radius. If this is the case, the most recently sampled nucleon is rejected. This treatment, however, distorts the W-S distribution and the W-S parameters must be retuned so that the correct final distribution is obtained after applying the exclusion radius. However, the effects from the inclusion of the more realistic 2-nucleon correlations are expected to be relatively small in the measurable quantities considered in this thesis [96, 97]. Thus, here the 2-nucleon correlations are not taken into account in any way.

After the nuclear configurations for the colliding nuclei A and B have been

obtained, the impact parameter is sampled from a distribution

$$\frac{dN}{db} \sim b. \tag{3.12}$$

Next the collisions between nucleons from A and B are determined. A simple hard-sphere modeling is applied here: a nucleon i from A and a nucleon j from B are assumed to collide if

$$(x_i - x_j)^2 + (y_i - y_j)^2 \leq \frac{\sigma_{NN}}{\pi}. \tag{3.13}$$

After all nucleon pairs have been considered, the number of BC and WN and their transverse positions are known. One Au+Au event is plotted in Fig. 3.2.

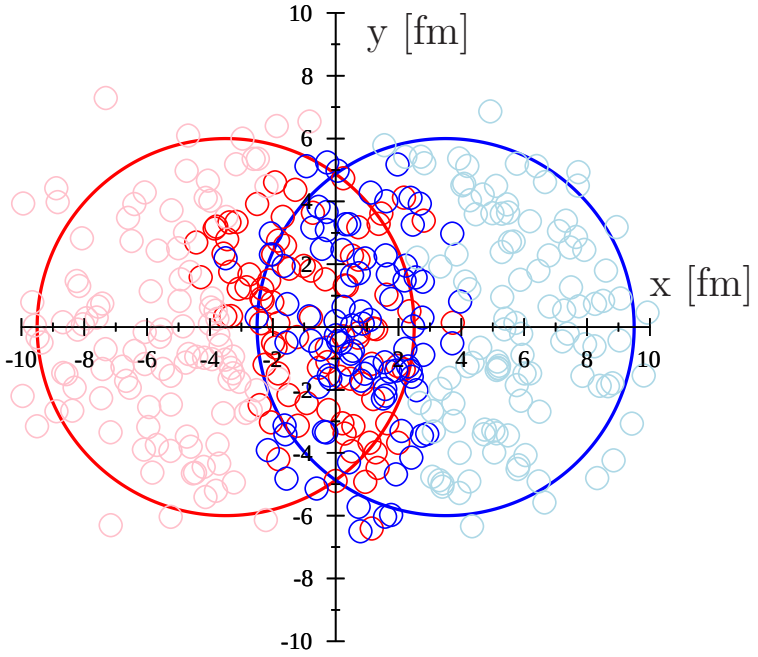

Figure 3.2: An example of the initial nucleon configurations in the MCG model. Nucleons with the light colors do not collide with the other nucleus. Here the nucleon radius is smaller than the hard-sphere collision radius.

Participants are plotted in red and blue and spectators are plotted with pink and light blue. Note that the nucleon radius in the figure is smaller than the hard-sphere collision radius.

When the initial states for hydrodynamics are constructed, the energy density profiles must be generated from the positions of the wounded nucleons or binary collisions. A simple way to do this is to use a 2-dimensional Gaussian smearing around the positions. The energy density is then

$$\epsilon(x,y) = \frac{K}{2\pi\sigma^2} \sum_{i=1}^{N_{\mathrm{part}} \text{ or } N_{\mathrm{bin}}} \exp\Big(- \frac{(x-x_i)^2 + (y-y_i)^2}{2\sigma^2}\Big), \tag{3.14}$$

where σ is a free parameter controlling the width of the Gaussian and K is the overall normalization constant. With the above construction the distributed total energy does not depend on σ. However the total entropy S now scales as

$$S \sim \int dxdy\, \epsilon^{3/4}(x,y) \sim \sqrt{\sigma} \tag{3.15}$$

and thus different values for σ lead to different multiplicities. These initial states can be thought as event-by-event analogues of the previously mentioned eBC and eWN profiles. Naturally, also the entropy density can be distributed according to the WN or BC positions. If Eq. (3.14) is used in this case, the total entropy does not depend on σ, but the total energy does.

A smooth (averaged) profile can be obtained from the MCG model as an average over sufficiently many events. Since hydrodynamics needs the energy density profile as input, entropy-based initial states must be converted to energy density using the chosen EoS. When taking an average over entropy densities, one must decide if the EoS is used for each event before taking the average, or if the average is taken first and the EoS is used once after that.

3.3 Centrality classes

The centrality classes are defined in this thesis using the impact parameter for the optical Glauber model and the number of participants for the MCG model. In the optical Glauber case the total cross-section is

$$\sigma_{\mathrm{tot}}^{AA} = \int d^2\boldsymbol{b} \frac{d\sigma}{d^2\boldsymbol{b}} = \int d^2\boldsymbol{b} \Big(1 - e^{-T_{AA}(\boldsymbol{b})\sigma_{NN}^{\mathrm{in}}}\Big). \tag{3.16}$$

The centrality classes correspond to impact parameter ranges $[b_i, b_{i+1}]$, which are obtained so that the cross sections are a certain fraction c_i of the total cross section,

$$c_i = \frac{1}{\sigma_{\mathrm{tot}}^{AA}} \int_{b_i}^{b_{i+1}} d^2\boldsymbol{b} \Big(1 - e^{-T_{AA}(\boldsymbol{b})\sigma_{NN}^{\mathrm{in}}}\Big). \tag{3.17}$$

The average impact parameter, number of particles and other average quantities for the centrality classes can then be calculated using the distribution $d\sigma/d^2\mathbf{b}$ as a weight.

In the MCG case the centrality classes could be defined in the same way. However, the amount of initial entropy is proportional to the number of participants (or binary collisions) in the MCG and thus it is more meaningful to use N_{part} (N_{bin}) instead of the impact parameter. Thus the distribution of N_{part} is sliced into intervals containing a certain fraction of total number of events. For example in Fig. 3.3 is shown how the centrality classes are determined in Au+Au collisions at $\sqrt{s_{NN}} = 200$ GeV.

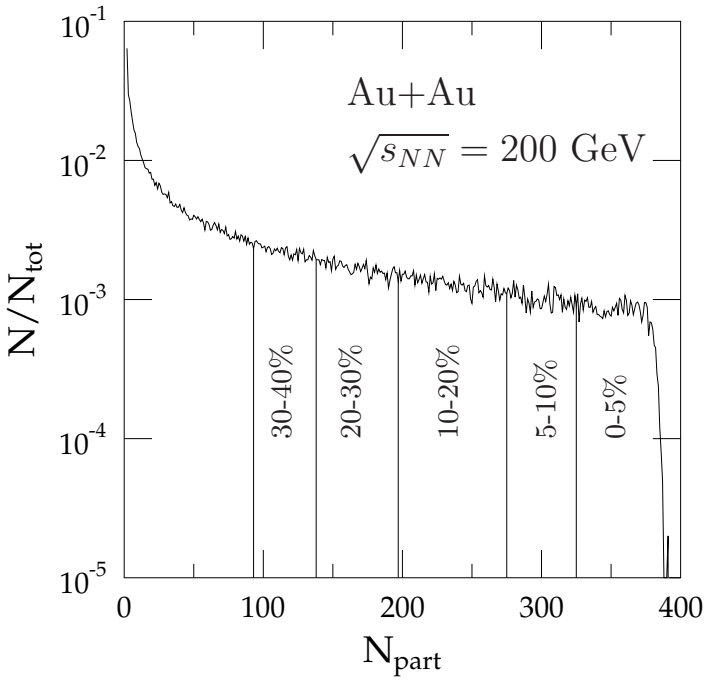

Figure 3.3: Definition of the centrality classes with MCG. This example is for Au+Au collisions at $\sqrt{s_{NN}} = 200$ GeV. From [I].

3.4 Eccentricity

The initial eccentricity, $\epsilon\{\mathrm{RP}\}$, which describes the ellipticity of the initial matter distribution, is defined as

$$\epsilon\{\mathrm{RP}\} = \frac{\langle y^2 - x^2 \rangle}{\langle y^2 + x^2 \rangle}. \tag{3.18}$$

Here the average $\langle \dots \rangle$ can be over wounded nucleons, binary collisions or energy density. During the hydrodynamical evolution this spatial anisotropy is transferred into a momentum anisotropy and finally the eccentricity can be related to the elliptic flow as will be discussed later in this thesis.

In the smooth initial states, the collision area has a nice almond shape as can be seen from Fig. 3.1. When the event-by-event fluctuations in the nucleon positions are included, it may happen that the overlap almond seems to be rotated by some angle. This means that a larger eccentricity is obtained if the coordinate axis are tilted accordingly. An example of this can be found in Fig. 3.4.

If the system is rotated by an angle α, the new coordinates are

$$\begin{aligned} x' &= x\cos\alpha - y\sin\alpha \\ y' &= x\sin\alpha + y\cos\alpha. \end{aligned} \tag{3.19}$$

In this case the eccentricity is

$$\epsilon'(\alpha) = \frac{\langle y^2 - x^2 \rangle(\cos^2\alpha - \sin^2\alpha) + 4\langle xy\rangle \sin\alpha\cos\alpha}{\langle y^2 + x^2 \rangle}. \tag{3.20}$$

From this one can find the angle that maximizes the $\epsilon'(\alpha)$. The derivative has two possible zeros at

$$\tan\alpha = \frac{2\langle xy\rangle}{\langle y^2 - x^2\rangle + S} \tag{3.21}$$

where

$$S = \pm\sqrt{\langle y^2 - x^2\rangle^2 + 4\langle xy\rangle^2}. \tag{3.22}$$

Now the zeros of the derivative can be expressed with

$$\begin{aligned} \sin\alpha &= \frac{2\langle xy\rangle}{\sqrt{2(S^2 + \langle y^2 - x^2\rangle S)}} \\ \cos\alpha &= \frac{\langle y^2 - x^2\rangle + S}{\sqrt{2(S^2 + \langle y^2 - x^2\rangle S)}}. \end{aligned} \tag{3.23}$$

After inserting these into Eq. (3.20) the largest possible eccentricity is [98]

$$\epsilon\{\mathrm{PP}\} = \epsilon'(\alpha) = \stackrel{+}{(-)}\frac{\sqrt{\langle y^2 - x^2\rangle^2 + 4\langle xy\rangle^2}}{\langle y^2 + x^2\rangle}, \tag{3.24}$$

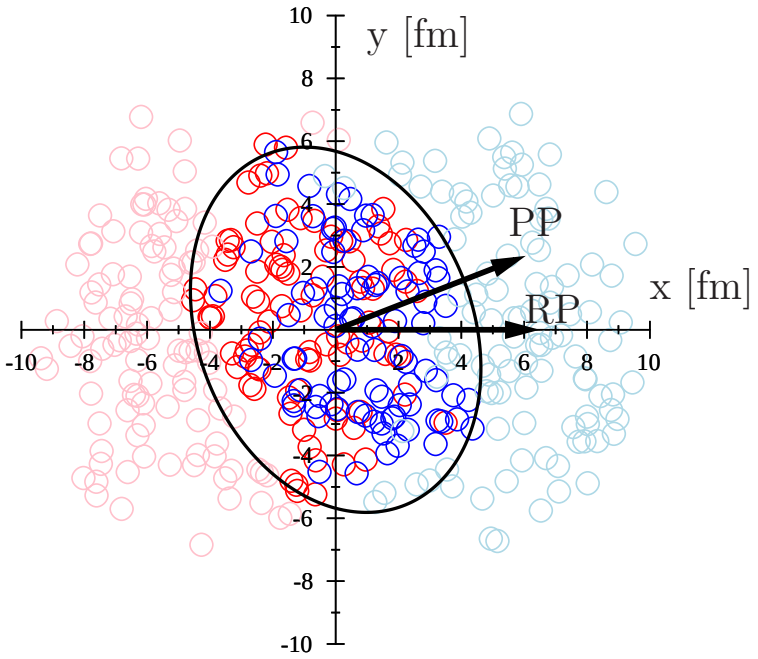

Figure 3.4: A MCG event, where the maximal eccentricity is obtained when the coordinate axes are tilted by an angle ψ_{PP}. To guide the eye, I have drawn an ellipse which has been tilted accordingly and whose eccentricity matches the one calculated from the participants. Also the reaction and participant planes are shown.

which is usually called participant eccentricity. This value is achieved when the coordinate axis of the system are rotated by an angle

$$\psi_{\mathrm{PP}} = \arctan \frac{-2\langle xy \rangle}{\langle y^2 - x^2 \rangle + \sqrt{\langle y^2 - x^2 \rangle^2 + 4\langle xy \rangle^2}}. \tag{3.25}$$

Here the ψ_{PP} and the z-axis define the participant plane (PP).

Figure 3.5 shows the comparison between $\epsilon\{\mathrm{RP}\}$ and $\epsilon\{\mathrm{PP}\}$. As expected, the participant eccentricity is always larger since it is the largest eccentricity by definition. The difference between these two eccentricities is largest in most central and in very peripheral collisions. In central collisions the impact parameter is so small that not much anisotropy is created. Thus the fluctuations are the most

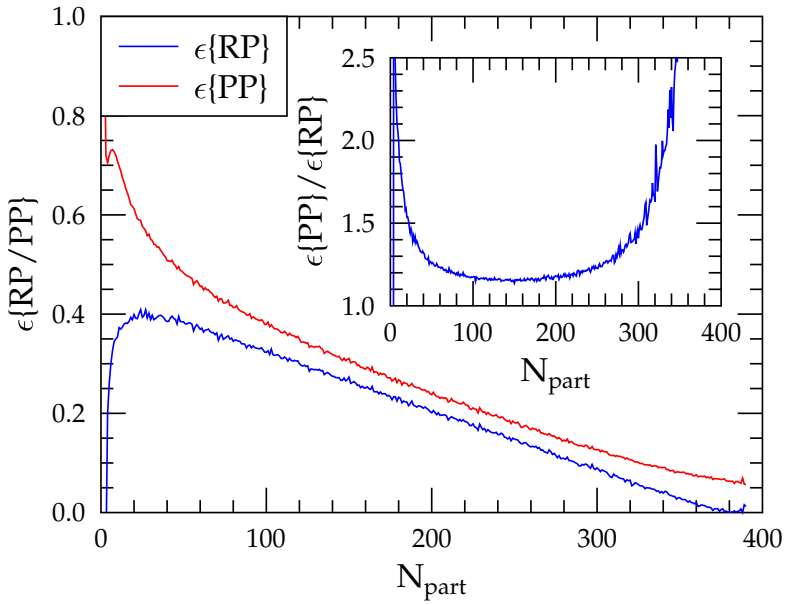

Figure 3.5: A comparison between the eccentricities calculated with respect to the RP and PP as a function of N_{part}.

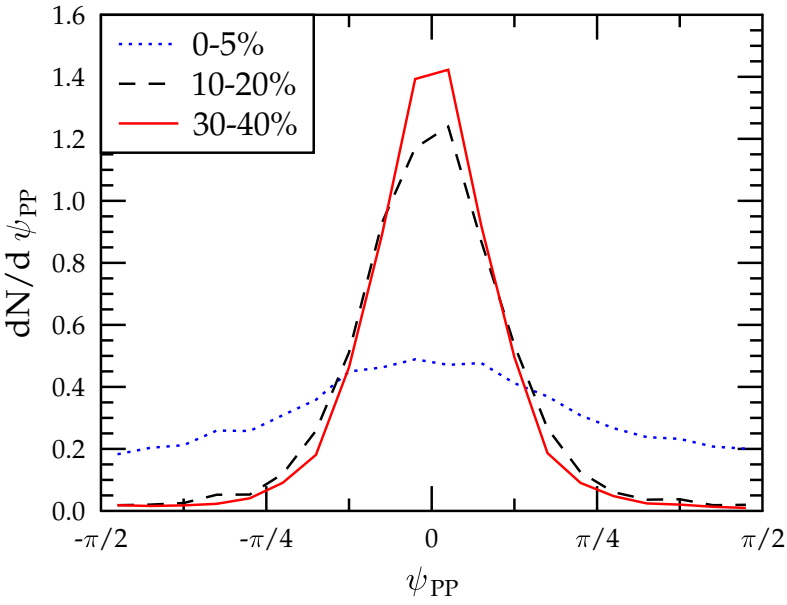

Figure 3.6: Distribution of PP angles in three different centrality classes. These distributions are for Au+Au collisions at $\sqrt{s_{NN}} = 200$ GeV.

important source of eccentricity there. In the very peripheral collisions the system size is so small that the fluctuations are again very important. However, it should be pointed out that the validity of the hydrodynamical description eventually breaks down in the very peripheral collisions.

The angular distribution of the PP angles is plotted in Fig. 3.6. If this figure is studied together with Fig. 3.5, one can see that in central collisions the distribution of the PP angles is very wide and the difference between two eccentricities may be large. Thus if the plane which maximizes the eccentricity is far away from the RP one can assume that $\epsilon\{\mathrm{RP}\}$ is much smaller. Around $N_{\mathrm{part}} \sim 100 - 250$, which corresponds to the 10-20%, 20-30% and 30-40% centrality classes, the eccentricities are quite close to each other and the PP angle distribution is much narrower. Since PP is always close to RP, also the eccentricities must be close to each other.

3.5 Comparison between Optical Glauber and MCG models

The optical and Monte Carlo versions of the Glauber model should in principle describe the same physical process and the results should be the same. However, there exists some differences due to the different assumptions. In this section these two models are compared and some of the differences are pointed out.

The geometrical cross section $d\sigma/db$ as a function of the impact parameter is plotted in Fig. 3.7. From here one sees that the total cross section is slightly larger in the optical Glauber model. This will naturally lead to different centrality class definitions even if the impact parameter would be used in both cases to define the centrality classes. Table 3.1 shows various centrality classes for the RHIC and LHC calculations considered in this thesis, calculated from the optical Glauber model using the b-slicing. The inelastic nucleon-nucleon cross section is taken to be 42 (64) mb for $\sqrt{s_{NN}} = 200$ (2760) GeV. Table 3.2 contains the same centrality classes calculated in the MCG model with N_{part} slicing. While the values of $\langle b \rangle$ agree fairly well, the differences in N_{bin} and N_{part} are small in most central collisions, but the discrepancy increases towards more peripheral collisions. In 0-5% (50-60%) centrality class the difference in N_{part} is $\sim 2\%$ (20%).

Finally the eccentricity of the energy density distribution with respect to the reaction plane is plotted in Fig. 3.8 from the optical Glauber model as well as from the smooth MCG initial state, which is obtained by taking average over 10 000 events. The difference between these two models is surprisingly large. Difference is roughly 30% and it stays approximately constant at all centralities considered here. The largest contribution to the eccentricity is coming from the edges of the collision area, where the differences between the optical Glauber and MCG models

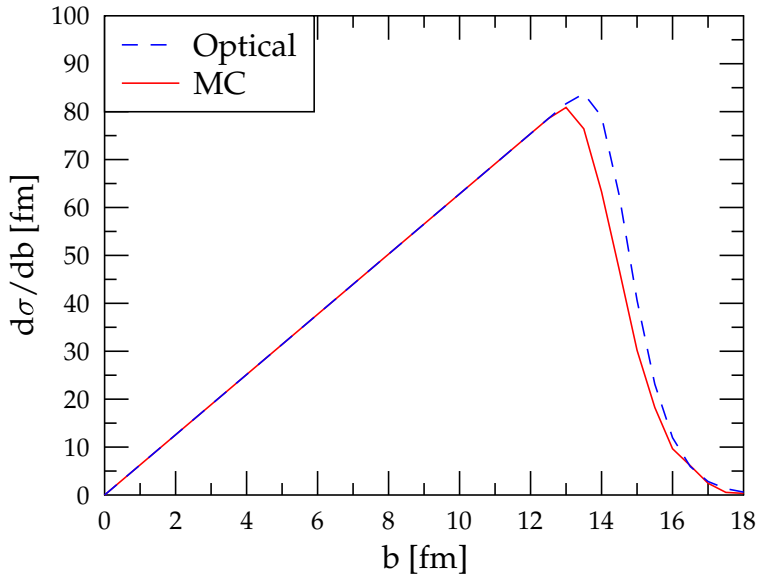

Figure 3.7: The cross section from the optical and Monte Carlo Glauber models in Au+Au collisions at $\sqrt{s_{NN}} = 200$ GeV as a function of impact parameter.

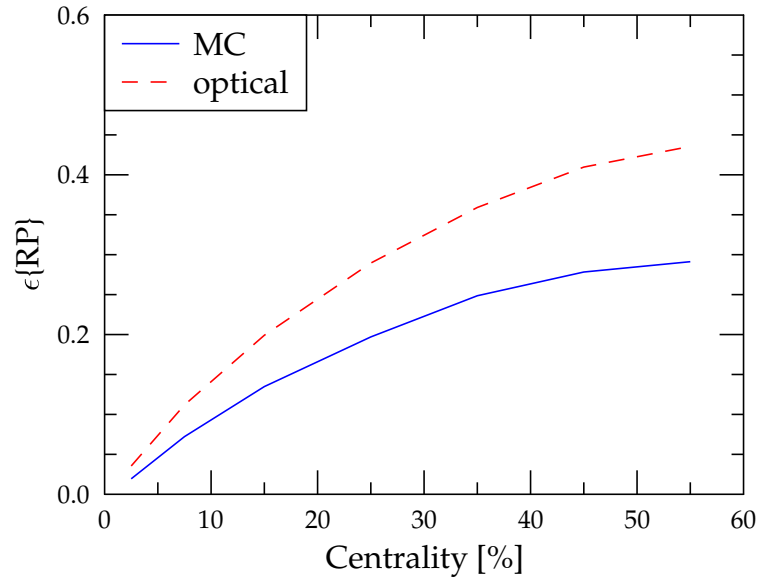

Figure 3.8: The reaction plane eccentricity from the optical and Monte Carlo Glauber models in Au+Au collisions at $\sqrt{s_{NN}} = 200$ GeV as a function of centrality.

	centrality %	b range [fm]	$\langle b \rangle$ [fm]	$N_{\rm part}$	$N_{\rm bin}$
	0-5	0.00-3.35	2.24	346	1080
	5-10	3.35-4.74	4.08	289	844
	10-15	4.74-5.81	5.30	242	662
	15-20	5.81-6.71	6.27	202	518
	20-30	6.71-8.21	7.49	153	355
RHIC	30-40	8.21-9.49	8.87	102	203
	40-50	9.49-10.6	10.1	64.4	107
	50-60	10.6-11.6	11.1	37.5	51
	0-20	0.00-6.71	4.47	267	777
	20-40	6.71-9.49	8.18	128	279
	0-5	0.00-3.53	2.35	375	1710
LHC	0-20	0.00-7.05	4.70	294	1213
	20-40	7.05-9.98	8.60	141	423

Table 3.1: Various centrality classes for Au+Au collisions at $\sqrt{s_{NN}} = 200$ GeV and for Pb+Pb collisions at $\sqrt{s_{NN}} = 2.76$ TeV, obtained from the optical Glauber model.

	centrality %	$N_{\rm part}$ range	$\langle b \rangle$ [fm]	$N_{\rm part}$	$N_{\rm bin}$
	0-5	394 - 325	2.25	353	1070
	5-10	324 - 275	4.07	299	843
	10-15	274 - 232	5.27	252	665
	15-20	231 - 196	6.23	213	525
	20-30	196 - 138	7.40	166	370
RHIC	30-40	137 - 93	8.76	114	218
	40-50	92 - 59	9.94	74.6	120
	50-60	58 - 34	11.0	45.2	59.7
	0-20	394 - 197	4.44	280	778
	20-40	196 - 93	8.08	140	294
	0- 5	416 - 357	2.32	384	1690
LHC	0-20	416 - 221	4.64	309	1220
	20-40	220 - 104	8.52	157	441

Table 3.2: Various centrality classes for Au+Au collisions at $\sqrt{s_{NN}} = 200$ GeV and for Pb+Pb collisions at $\sqrt{s_{NN}} = 2.76$ TeV, obtained from the Monte Carlo Glauber model.

can be expected to be largest. Since in the MCG model the number of nucleons is small on the edge of the nucleus, the effect of fluctuations is large. In the center of the collision area the number of nucleons is larger and the difference to the smooth nuclear density is smaller.

3.6 EKRT model

In the previous sections I have described how the initial transverse profile for energy or entropy density can be obtained. However, additional input is still needed before hydrodynamical calculations can be made. The overall normalization, K in equations (3.11) and (3.14), can be always fixed by fitting to the measured multiplicity, but in that case predictions for higher energies cannot be made. Another, even more crucial, input is the initial time τ_0, which cannot be fixed from the data uniquely. In this thesis both the initial normalization and the initial time are taken from the EKRT model [23].

The EKRT model is based on a pQCD mini-jet calculation and on a gluon saturation criterion in the transverse plane. Each mini-jet production vertex occupies a geometric uncertainty area $\sim \pi/p_T^2$ and when these areas start to overlap, the saturation of primary parton production (almost solely gluons) is expected to take place. At the saturation

$$N(p_{\rm sat})\pi/p_{\rm sat}^2 = \pi R_A^2, \tag{3.26}$$

where $N(p_{\rm sat})$ is the number of mini-jets produced with $p_T \geq p_{\rm sat} \gg \Lambda_{\rm QCD}$ at the mid-rapidity unit $\Delta y = 1$. The number of the mini-jets is calculated from

$$N(p_{\rm sat}) = T_{AA}(\mathbf{0})\sigma\langle N\rangle \tag{3.27}$$

where $\sigma\langle N\rangle$ is essentially the integrated leading-order (LO) pQCD cross section (see e.g. [99, 100] for details). For the produced transverse energy (E_T) this pQCD calculation has been extended to the next-to-leading order (NLO) in an infra-red and collinear singularity safe way [101]. The number of the mini-jets is, however, a well defined quantity only in the LO and thus the K-factors from the E_T calculation are used also for $N(p_{\rm sat})$ appearing in the saturation criterion [101].

The formation time of the system is $\tau_f \sim 1/p_{\rm sat}$ and here it is assumed that the system is also thermalized at the same time. Thus the hydrodynamical evolution is started at $\tau_0 = 1/p_{\rm sat}$. The system may have not fully thermalized so early, but it starts to have collective behavior (e.g. flow) right from the formation. Thus starting at $\tau_0 = \tau_f$ the initial flow can be set to zero quite safely.

In what I discuss here, the EKRT model is considered only for central collisions. In this case the total transverse energy of the mini-jets is $E_T = \sigma\langle E_T\rangle T_{AA}(\mathbf{0})$, where $\sigma\langle E_T\rangle$ is the first moment of the mini-jet E_T distribution. Then following

Refs. [99, 100] the energy density can be written as

$$\epsilon(x, y, \tau_0) = \frac{\sigma\langle E_T\rangle}{\tau_0 \Delta y} T_A(x, y) T_B(x, y). \tag{3.28}$$

From this density distribution one can calculate the total energy (or entropy) for hydrodynamics in the case $b = 0$ fm. In this thesis the transverse profiles are obtained from different Glauber models while the overall normalization constants in Eqs. (3.11) and (3.14) are fixed so that the amount of energy (entropy) with $b = 0$ fm is equal to the amount given by Eq. (3.28) [102].

Chapter 4

Hydrodynamical flow

In the 90s the elliptic flow, which describes the anisotropy of the final particle transverse momentum distributions, was proposed to be a signature of the collective behavior in URHIC [103]. The idea is that a particle spectrum can be written as a Fourier series

$$\frac{dN}{d^2p_T dy} = \frac{1}{\pi}\frac{dN}{dp_T^2 dy}\Big(1 + 2\sum_{n=1}^{\infty} v_n \cos(n\phi)\Big), \tag{4.1}$$

where ϕ is the azimuthal angle of the particle's transverse momentum with respect to a chosen reference plane and v_n is the Fourier coefficient for the n^{th} harmonic. The elliptic flow is the second harmonic v_2.

Recently the fluctuations in the initial state have been studied in more detail and it has been realized that also events with triangular shape exist and this phenomenon can be measured as v_3 [104]. Also higher harmonics have now been measured up to v_6 [105]. The higher harmonics have proved to be useful observables in constraining the QCD matter shear viscosity [63, 106].

The flow coefficients can be measured with many different methods. The event plane (EP) method [107], which is also considered in this thesis, is one of the most traditional methods. Also the cumulants constructed from the n-particle correlations can be used to measure the flow coefficients [108–110]. Usually 2- and 4-particle cumulants are applied in the experimental data analysis. Another commonly used approach is the Lee-Yang zeros (LYZ) method [111, 112].

All of these methods have a different response to the flow fluctuations and non-flow effects (e.g. resonance decays produce particle correlations, which can be mistakenly interpreted as flow) and thus the values for the flow coefficients need not be exactly same for each method [113]. Because of this, one should be very careful in that the comparisons between the theory and the experiments are done with consistent methods. Since the event-by-event framework presented in this thesis has individual hadrons in the final state, we can apply the same flow

analysis methods as in the experiments. This allows us to make a more meaningful one-to-one comparison of v_n with the experimental data.

4.1 Event plane method

Let us consider the event plane method [107], which has been widely used in the experimental flow analysis. First the event flow vector $\boldsymbol{Q}_n$ for the n^{th} harmonic is calculated for each event as

$$\boldsymbol{Q}_n = \sum_i (p_{Ti}\cos(n\phi_i), p_{Ti}\sin(n\phi_i)), \tag{4.2}$$

where p_T is used as a weight and i runs over the particles in the event. The best weight would be v_n itself, but the p_T is fine for the harmonics studied in this thesis, since the v_2 and v_3 grow with p_T in the hydrodynamical region. For example v_1 coefficient at the mid-rapidity needs a different weight in order to be observed [114, 115].

The event plane angle for the n^{th} harmonic is obtained from $\boldsymbol{Q}_n$ as

$$\psi_n = \frac{\arctan(Q_{n,y}/Q_{n,x})}{n}, \tag{4.3}$$

where the arctan is placed in the correct quadrant so that the EP angle is always in the range $[-\pi/n, \pi/n]$. The "observed" v_n can then be calculated using the obtained angle as the reference plane angle,

$$v_n\{\text{obs}\} = \langle\langle\cos(n(\phi_i - \psi_n))\rangle\rangle_{\text{events}}, \tag{4.4}$$

where the inner angle brackets denote an average over all particles i in one event and the outer ones an average over all events. The event plane angle is calculated separately for each event. If the same set of particles is used to determine the event plane and v_n, the particle of interest must be removed from the event plane calculation in order to remove the autocorrelations.

Since each event has only a finite number of particles from which the event plane angle can be determined, the angle will fluctuate around the "true" ψ_n, which would be determined from infinitely many particles. If the used rapidity interval is very small, events will have only a few hadrons from which the event plane can be determined. Then the fluctuations can be large and the obtained EP angle can deviate significantly from the "true" EP angle. In this case, due to the wash-out effect of these ψ_n fluctuations, the obtained v_n can become much smaller than the true physical value. If the same events are taken with a larger rapidity interval, the event planes will be closer to the "true" event plane and the obtained

v_n can deviate from the one obtained with the smaller interval. Thus the $v_n\{\text{obs}\}$ cannot be considered as a well-defined physical quantity.

However, a physical observable can be constructed from the $v_n\{\text{obs}\}$ by defining the event plane resolution,

$$\mathcal{R}_n = \langle \cos(n(\psi_n - \psi_n^{\text{true}}))\rangle, \tag{4.5}$$

where ψ_n^{true} is the true event plane and the average is over events. Then the event plane value for the harmonic n is

$$v_n\{\text{EP}\} = \frac{v_n\{\text{obs}\}}{\mathcal{R}_n}. \tag{4.6}$$

The resolution is one when the event plane is known very well (lots of particles, large anisotropy) and it decreases when the uncertainty in the EP angle determination increases (few particles, small anisotropy).

In principle the true EP could be obtained from the theory calculation, but it can never be measured. Since the aim here is to make a one-to-one comparison with the experiments, $\mathcal{R}_n$ needs to be obtained with the 2-subevent method [107]. In this method the event is divided into two equal subevents A and B. The event plane is then determined in both subevents and the resolution can be obtained as

$$\begin{aligned}\langle \cos(n(\psi_n^A - \psi_n^B))\rangle =& \langle \cos[n(\psi_n^A - \psi_n^{\text{true}} + \psi_n^{\text{true}} - \psi_n^B)]\rangle \\ \approx& \langle \cos[n(\psi_n^A - \psi_n^{\text{true}})]\rangle \langle \cos[n(\psi_n^B - \psi_n^{\text{true}})]\rangle \\ =& (\mathcal{R}_n^{\text{sub}})^2,\end{aligned} \tag{4.7}$$

assuming $\langle \sin[n(\psi_n^{A(B)} - \psi_n^{\text{true}})]\rangle \approx 0$. Since the subevents were equal, their resolution must be the same. Hence the subevent resolution can be obtained from the EP angles. However, the obtained $\mathcal{R}_n^{\text{sub}}$ cannot be used to correct $v_n\{\text{obs}\}$ from the full event, since the number of particles is different. Additional modeling is therefore needed before $\mathcal{R}_n$ can be obtained for the full event.

When the fluctuations are assumed to be Gaussian, the probability distribution of $\boldsymbol{v_n} = (v_n \cos\psi_n, v_n \sin\psi_n)$ in one event can be written as

$$\frac{dP}{dv_n d\psi} = \frac{1}{2\pi\sigma^2} \exp\Big[- \frac{\boldsymbol{v_n^2}}{2\sigma^2}\Big], \tag{4.8}$$

where the variance of the distribution is $\sigma^2 \sim 1/N$ and N is the number of particles. For each event the center of the distribution is shifted to the point where v_n and ψ_n get their true values v_n^{true} and ψ_n^{true}. Let us now consider the distribution with respect to the angle difference $n\psi_n' = n(\psi_n - \psi_n^{\text{true}})$. The integral over v_n can be

done and the result is [116, 117]

$$\begin{aligned}\frac{dP}{d(n\psi'_n)} =& \int_0^\infty dv_n \frac{v_n}{2\pi\sigma^2} \exp\Big[- \frac{v_n^2 + (v_n^{\rm true})^2 - 2v_n v_n^{\rm true}\cos(n\psi'_n)}{2\sigma^2}\Big] \\ =& \frac{1}{2\pi}\Big[\exp\Big(-\frac{(v_n^{\rm true})^2}{2\sigma^2}\Big) + \frac{\sqrt{\pi}v_n^{\rm true}\cos(n\psi'_n)}{\sqrt{2}\sigma}\times \\ & \exp\Big(-\frac{(v_n^{\rm true})^2\sin^2(n\psi'_n)}{2\sigma^2}\Big)\Big(1+{\rm erf}\Big[\frac{v_n^{\rm true}\cos(n\psi'_n)}{\sqrt{2}\sigma}\Big]\Big)\Big],\end{aligned} \tag{4.9}$$

where erf is the error function [55]. Next the resolution for a single event can be calculated as an average over the obtained distribution [116, 117]

$$\begin{aligned}\mathcal{R}_n =& \langle\cos(n\psi'_n)\rangle = \int_0^{2\pi/n} d(n\psi'_n)\cos(n\psi'_n)\frac{dP}{d(n\psi'_n)} \\ =& \frac{\sqrt{\pi}}{2\sqrt{2}}\chi_n \exp(-\chi_n^2/4)\Big[I_0(\chi_n^2/4) + I_1(\chi_n^2/4)\Big],\end{aligned} \tag{4.10}$$

where I_0 and I_1 are modified Bessel functions [55] and $\chi_n = v_n^{\rm true}/\sigma \sim \sqrt{N}$. Since the subevent resolution is known from Eq. (4.7), the $\chi_n^{\rm sub}$ can be solved for the subevents. Since the full event has twice the number of particles than the subevent, we have

$$\chi^{\rm full} = \sqrt{2}\chi^{\rm sub}. \tag{4.11}$$

Now, with the obtained $\chi^{\rm full}$, one can calculate the correction for the full event from Eq. (4.10).

The importance of the resolution correction is shown in Fig. 4.1, where central Au+Au collisions at $\sqrt{s_{NN}} = 200$ GeV are considered with different resolutions (rapidity intervals). In panel (a) I have plotted the $v_2\{\rm obs\}$ and one can clearly see that a larger resolution leads to a larger elliptic flow. This also demonstrates the previously argued unphysical nature of $v_2\{\rm obs\}$: the obtained $v_2\{\rm obs\}$ depends on the rapidity acceptance despite the fact that the longitudinal boost-invariance is assumed.

The panel (b) shows the $v_2\{\rm EP\}$ and from here one can see that every resolution gives essentially the same result. Actually by closer inspection one can see that the curves seem to be ordered so that the higher the resolution, the smaller the $v_2\{\rm EP\}$. Differences are here very small but the order of the curves can be understood since actually the event plane method gives $v_2\{\rm EP\} = \langle (v_2^{\rm true})^\alpha\rangle^{1/\alpha}$, where the power α depends on the resolution [113]. When the event plane is known very accurately (larger rapidity interval, more particles) $\alpha \approx 1$ and when the resolution is poor (smaller rapidity interval, less particles) $\alpha \approx 2$. Thus the $v_2\{\rm EP\}$ with small $\mathcal{R}_n$ should be larger than with $\mathcal{R}_n \approx 1$.

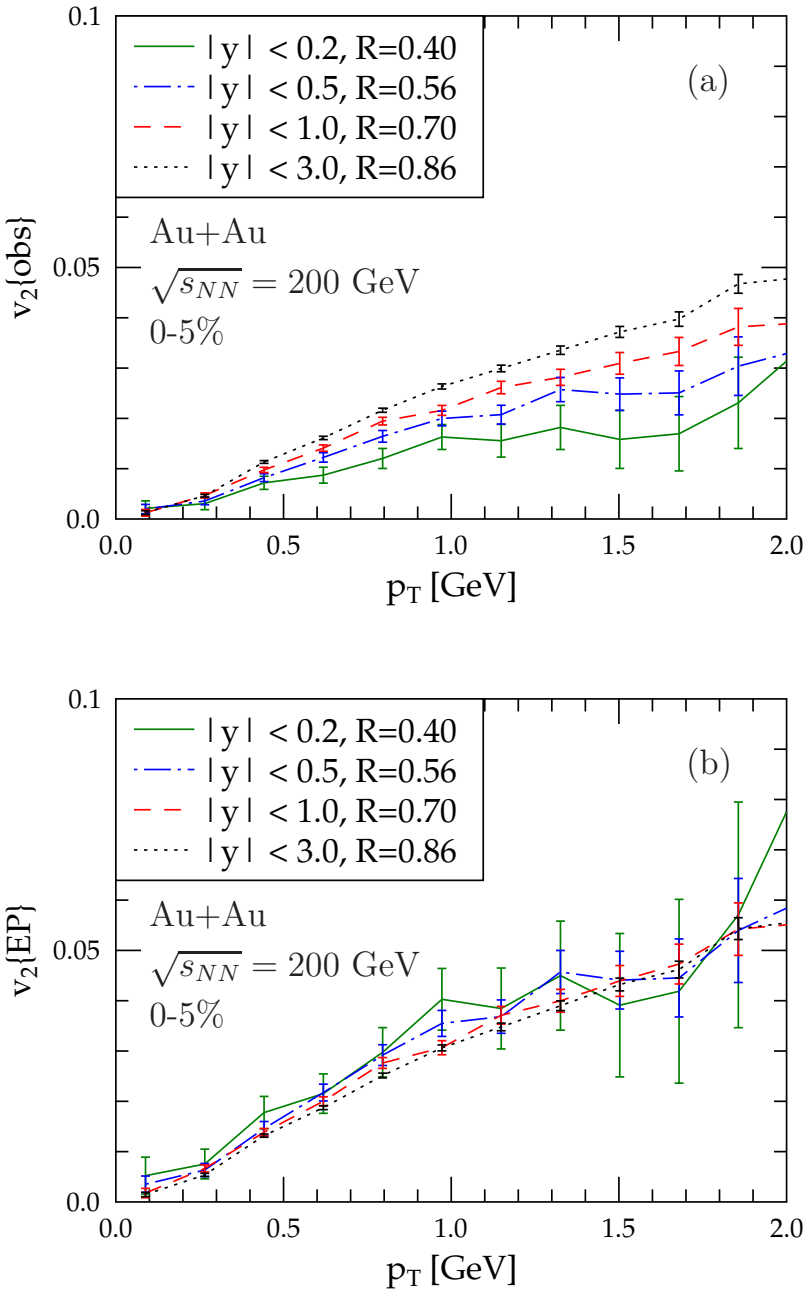

Figure 4.1: The elliptic flow with respect to the event plane as a function of p_T using different rapidity intervals in 0-5% central Au+Au collisions at $\sqrt{s_{NN}} = 200$ GeV. In panel (a) no correction from the EP fluctuations has been made and in panel (b) the corrections are included.

4.2 Initial state anisotropies and final flow coefficients

The flow coefficients measured from the final state are obviously closely linked to the initial state anisotropies. Since the hydrodynamical calculations are usually started with zero transverse flow, all of the flow must be generated during the hydrodynamical expansion. If smooth initial conditions are considered, the initial density distribution has a nice almond shape with non-tilted main axes, when the impact parameter is non-zero. It is obvious that the pressure gradients are then larger in the direction of the x-axis than in the direction of the y-axis. Hence it is clear that the flow is stronger in the direction of x-axis and the final momentum distribution will become anisotropic.

With the initial state fluctuations the system is more complex, but again the initial eccentricity is converted into elliptic flow. In Fig. 4.2 I show a scatter plot of the eccentricity and elliptic flow in semi-peripheral Au+Au events. Here a large rapidity interval is used in order to determine the physical v_2 more accurately from each event. From the figure one can conclude that also when the initial density fluctuations are present, $v_2\{\mathrm{PP}\}$ is quite well correlated with ϵ_{PP}.

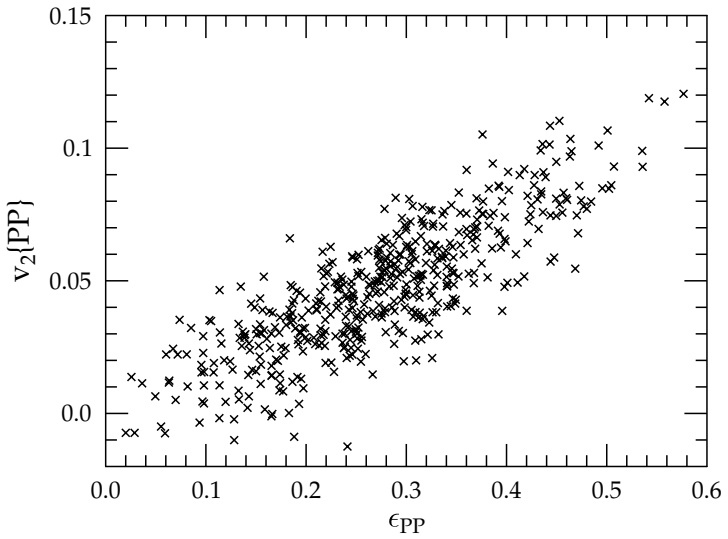

Figure 4.2: A scatter plot of the eccentricity and elliptic flow in 20-30% central Au+Au collisions at $\sqrt{s_{NN}} = 200$ GeV. Both quantities are calculated with respect to the participant plane.

Chapter 5

Thermal photons and hard partons as a medium probe

Photons are a highly interesting probe of the QCD matter produced in URHIC, since they can escape from the hot medium without interacting. This is due to the fact that the electromagnetic coupling is weak compared to the strong coupling. Thus the photons provide information about the system at the time they were produced, unlike hadrons which probe only the freeze-out region.

The photon measurements, however, are complicated since hadron decays form a huge background. The most dominant source of decay photons is π^0 which decays into two photons with the probability of 98.8% [1]. Since the electromagnetic coupling is small, the number of direct photons is small compared to hadrons and thus in the measurements the rare photonic probes must be found from the dominating background.

High energy partons, which are observed as jets in p+p collisions, cannot escape from the medium as easily as photons. At RHIC it was discovered that the high-p_T hadron production is suppressed, which can be explained by the fact that partons must traverse through the medium and lose energy in the interactions with it. Such "jet-tomography" can be used to study the medium properties. These two examples show that there is hope to constrain the medium parameters also by studying other probes which are not directly related to the small-p_T hadrons.

In this thesis I focus only on the photons produced by thermal emission from the hydrodynamical medium. First elliptic flow of thermal photons and its relation to the measurable direct photon v_2 are considered with smooth initial density profiles and after that I study the effects of the density fluctuations in the thermal photon p_T-spectra. In the end of this Chapter I briefly discuss the suppression of the high-energy partons as an application of the hydrodynamical framework developed in this thesis.

5.1 Thermal photons from hydrodynamical evolution

Emission of thermal photons from the hydrodynamical medium can be computed using the emission rates $\Gamma(E^*(x), T(x))$, where $E^* = p^\mu u_\mu(x)$ is the photon energy in the local rest frame of the fluid. The p_T spectrum of the thermal photons is obtained by integrating the emission rates over the entire hydrodynamical medium as

$$\frac{dN^\gamma}{d^2p_T dY} = \int d^4x\, \Gamma\Big(E^*(x), T(x)\Big), \tag{5.1}$$

where d^4x is the 4-volume element. The emitted photon yield from a single volume element thus depends on the temperature and flow. The emission rates have an exponential temperature dependence and thus the hot fluid cells emit much more photons than the colder ones. As discussed below, the hydrodynamical flow is also important for the photon emission.

Figure 5.1 shows the effect arising from the collective flow. The photons emitted from the plasma are not much affected by the flow since the emission is dominated

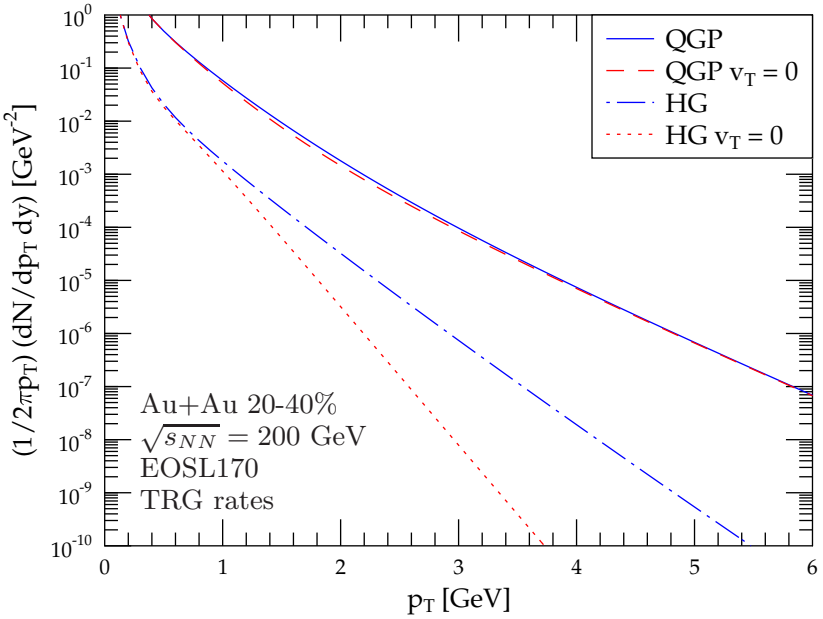

Figure 5.1: The effects of hydrodynamical flow in the transverse momentum spectra of thermal photons emitted from the QGP and HG in 20-40% central Au+Au at $\sqrt{s_{NN}} =$ 200 GeV.

by the hot regions at the early times, where not much flow has been developed. However, the photon spectra from the HG are very different with and without flow. The HG phase emission is mostly coming from a large volume at late times, where the transverse flow is already large. Thus the emitted photons get a boost to higher p_T from the transverse flow. The photons are emitted isotropically in the fluid's rest frame, but the boosts cause the photon p_T-distribution to be anisotropic when the impact parameter is non-zero or when the density fluctuations are present [92, 118, 119].

5.1.1 Emission rates

As was mentioned above, the photon emission rates are needed in order to perform the thermal photon calculations. These rates are obtained from rather tedious thermal field theory calculations, whose details are well beyond the scope of this thesis. The emission rates are different for the plasma and hadron gas and hence one would need to know the fractions of the QGP and HG matter in the medium at a given energy density. When the eosQ is used, the fractions of QGP and HG are always well defined due to the Maxwell construction in the mixed phase. However, when one uses the eosL, or some other EoS which has a cross-over phase transition, the fractions are not known. Thus additional uncertainty arises from the phase transition region unless the QGP and HG emission rates are very similar.

For the QGP emission the rate from Arnold, Moore and Yaffe [120, 121] is applied here. This rate depends on the strong coupling constant and here the choice for the running of the coupling is [122] $\alpha_s = \beta/\ln(8T/\Lambda)$, with $\beta = 6\pi/(33-2N_f)$, $\Lambda = 200$ MeV and $N_f = 3$. For the HG emission two different rates are used. The first ones are from Refs. [123–125]. These rates are denoted here as "R92". In addition, more recent rate parameterizations from Appendix A of Ref. [126] are used. The latter rates, which include also the hadronic form factors, we call "TRG" rates. In Fig. 5.2 the absolute rates are plotted as a function of the photon energy at $T = 170$ MeV.

As discussed above, the cross-over phase transition in the eosL causes some problems in the thermal photon calculations. From Fig. 5.3 it is obvious that it does matter which emission rate (plasma or HG) is used, since only the R92 rates are equal to the plasma rate around $E = 1$ GeV. Instead of using some arbitrary smooth transition for the plasma and HG phase fractions, a sudden transition at a certain temperature T_s is assumed here. To get a hold on the remaining uncertainty in the calculation, we study two "extreme" cases, $T_s = 170, 200$ MeV, and label them as "eosL170" and "eosL200".

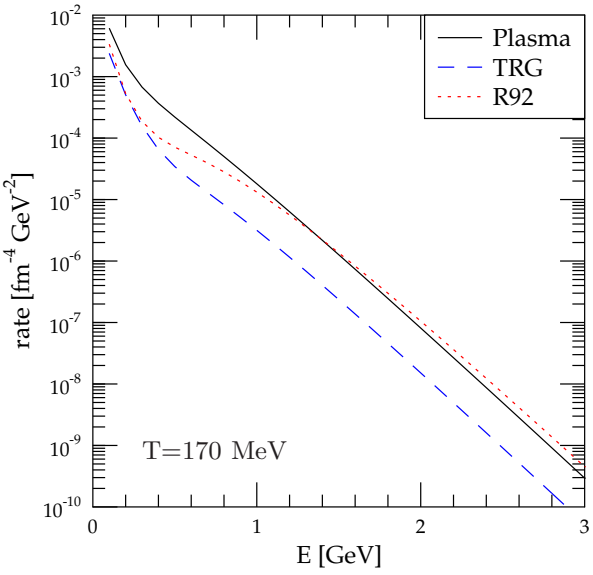

Figure 5.2: The different photon emission rates as a function of the photon energy at $T = 170$ MeV.

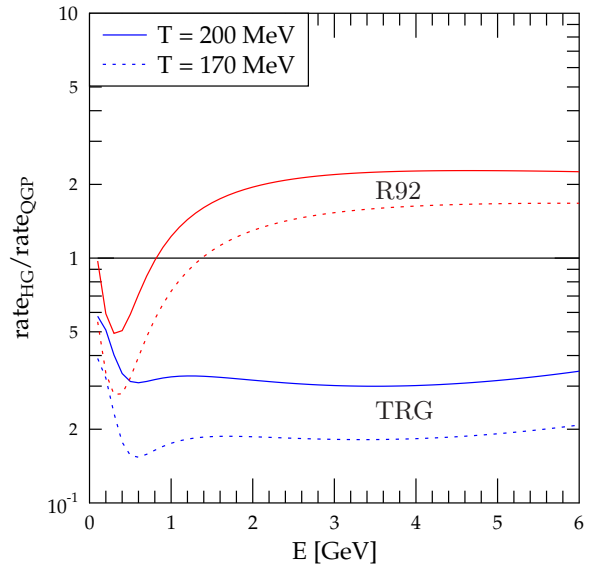

Figure 5.3: The ratio of the hadron gas and plasma emission rates of photons at two different temperatures. From [V].

5.2 Other sources of photons

In URHIC there exists also other mechanisms for direct photon production in addition to the thermal emission. The prompt photons (see e.g. [127]), which are produced in the primary interactions of the nucleons, are present in p+p collisions as well as in $A + A$ collisions. Since the prompt photons most likely do not interact with the medium, in nuclear collisions one should see just a superposition of $N_{\rm bin}$ p+p collisions, but naturally the nuclear effects in the parton distributions functions must be included [128, 129].

Another component that is present both in p+p and $A + A$ collisions are the fragmentation photons, which are emitted from the produced high-energy partons through the fragmentation process. However, the situation in $A + A$ collisions is now different from p+p collisions, since the partons interact with the medium, which is present only in the $A + A$ case. The prompt and fragmentation photons dominate the high-p_T part ($p_T \gtrsim 5$ GeV at RHIC) of the direct photon spectra in heavy ion collisions [130].

Also a jet-medium component, which is caused by the hard parton interactions with the medium, exists in URHIC. The high-energy quarks traversing through the medium can produce photons via the jet-photon conversion [131, 132] and in addition the medium can induce photon emission (bremsstrahlung) from the propagating parton. These components are expected to be most important in the intermediate p_T-region $\sim 3 - 5$ GeV [130, 133, 134].

5.3 Elliptic flow of photons

Elliptic flow of photons is defined in the same way as that of hadrons. Since the number of direct photons is very small, the photon v_2 measurement recently published by the PHENIX Collaboration [135] used the EP from the charged hadrons as the reference plane. In the present work [V], however, only smooth initial conditions are used in the photon v_2 studies and thus only $v_2\{\mathrm{RP}\}$ is calculated. For this reason a direct one-to-one comparison with the data cannot be made yet [136].

In this thesis, I study only the thermal photon component and thus a direct comparison with the v_2 data cannot be made since the thermal photons alone do not necessary fit the transverse momentum spectra at any p_T [1]. It is, however, possible to make a fit to the measured photon spectra and assume that the difference between the fit and the thermal photons are due to the other photon production mechanisms [V].

[1] See, however, the photon spectra with initial state density fluctuations in Fig. 6.10 and in Ref. [III].

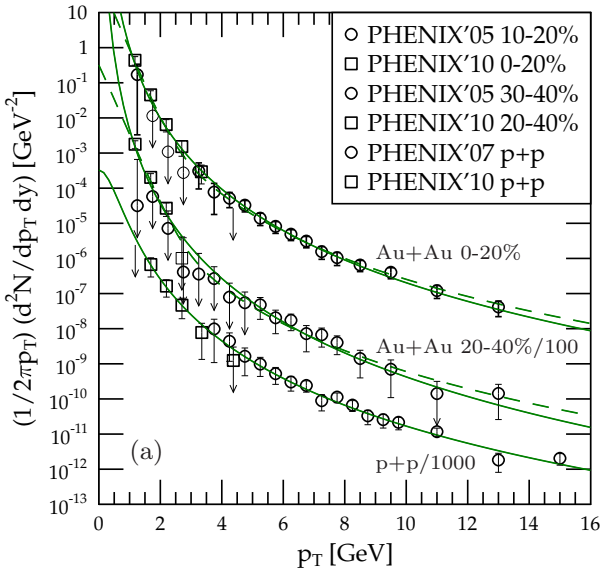

Figure 5.4: Direct photon transverse momentum spectra in Au+Au collisions and p+p collisions at $\sqrt{s_{NN}} = 200$ GeV measured by PHENIX Collaboration [137–139] and the fits given by Eqs. (5.3) and (5.4). From [V].

The prompt photons should not have a v_2 since they are produced in the primary interaction. The fragmentation photons, however, have a positive v_2 since the hard partons lose energy to the medium and develop a positive elliptic flow. Photons coming from the jet-medium interactions in turn have a negative v_2, since the probability to produce a photon is larger when there is more medium that a parton must traverse through. Thus the contribution to the v_2 from the other components partially cancels out. In Ref. [134] it was shown that the overall v_2 from these other components is expected to be very small.

The direct photon elliptic flow can thus be estimated using the thermal photon calculation and a fit to the measured transverse momentum spectra [V]. Assuming that all of the other components are emitted isotropically, the direct photon v_2 can be obtained as

$$\begin{aligned} v_2(p_T) &= \Big(\int d\phi \cos(2\phi) \frac{dN^{\mathrm{th}}}{dp_T^2 d\phi dy} \Big) \Big(\int d\phi \frac{dN^{\mathrm{fit}}}{dp_T^2 d\phi dy} \Big)^{-1} \\ &= v_2^{\mathrm{th}}(p_T) \Big(\frac{dN^{\mathrm{th}}}{dp_T^2 dy} \Big) \Big(\frac{dN^{\mathrm{fit}}}{dp_T^2 dy} \Big)^{-1}, \end{aligned} \tag{5.2}$$

where $dN^{\mathrm{fit}}/dp_T^2 dy$ is the total spectrum of photons, which is in this case obtained

by fitting the measured data. Correspondingly, $dN^{\rm th}/dp_T^2dy$ is the thermal photon spectrum and $v_2^{\rm th}$ is the elliptic flow from thermal photons alone. In Ref. [V] two different fit functions were used: Fit 1 is a sum of an exponential and a power law function [139],

$$f(p_T) = A\exp(-p_T/T) + \frac{C}{(1+p_T^2/b)^n}, \tag{5.3}$$

and Fit 2 is a pure power law,

$$f(p_T) = \frac{C}{(1+p_T^2/b)^n}, \tag{5.4}$$

where A, T, C, b and n are the fit parameters. For more details, see Ref. [V]. The photon v_2 results obtained in Ref. [V] will be summarized in Chapter 6 ahead.

5.4 Parton energy loss

As already mentioned, the high energy partons, which are produced in primary parton collision inside the medium (but before the medium is formed), interact with the medium and as a consequence they lose energy. This phenomenon can be observed for example as a suppression of the high-p_T particle spectra. Usually the amount of suppression is measured with the nuclear suppression factor R_{AA}, which is defined as

$$R_{AA}(p_T, y, \phi) = \frac{dN_{AA}^i/dp_T dy d\phi}{\langle N_{\rm bin}/\sigma_{NN}\rangle\, d\sigma^{pp}/dp_T dy d\phi}, \tag{5.5}$$

where $\langle N_{\rm bin}\rangle$ is the average number of BC at a given centrality. Thus R_{AA} is one (mod the isospin and nuclear PDF effects) if the $A+A$ collision is just a superposition of $N_{\rm bin}$ p+p collisions and the smaller the R_{AA} is, the larger is the suppression. From the experimental point of view, R_{AA} needs a baseline p+p spectrum at the same $\sqrt{s_{NN}}$. For example in the first LHC R_{AA} measurements, the lack of a baseline p+p run caused a large systematic uncertainty [140], which was considerably decreased by the appropriate p+p baseline measurement [141].

In the ideal case, the hard partons probe the hydrodynamical medium and the plasma properties can be constrained with such jet-tomography. However, the energy loss mechanism is not fully understood and several theoretical models are on the market nowadays [142–151]. Systematic studies presented in Ref. [152] have shown that it is difficult to discriminate between the models only with ϕ-integrated $R_{AA}(p_T)$, but a more differential observable, $R_{AA}(p_T, \phi)$, is needed.

Due to the initial spatial asymmetry at non-zero impact parameters, the partons traversing in the direction of the y-axis have a longer pathlength inside the

medium than the partons going parallel to the x-axis. The partons, which have a longer path, lose more energy and thus the nuclear suppression is anisotropic in non-central collisions. This can be seen in the angular dependence of $R_{AA}(p_T, \phi)$ measured by the PHENIX Collaboration [153]. Theoretical models are more sensitive to $R_{AA}(p_T, \phi)$ than $R_{AA}(p_T)$: for example in the elastic energy loss case the angular dependence can be concluded to be too weak [154]. Also the first studies with initial density fluctuations have been performed in Ref. [155].

The energy loss results can be quite sensitive to the underlying hydrodynamical model. In the systematic study of Ref. [II] different ideal and viscous hydrodynamical backgrounds were used in the R_{AA} calculations. First the energy loss parameters were tuned so that $R_{AA}(p_T)$ in central collisions was reproduced and then the angular dependence was studied in non-central collisions. On the one hand, the jet-medium interaction parameter (specific to each model) obtained from fitting $R_{AA}(p_T)$ is sensitive to the hydrodynamical background. On the other hand, the spread between in-plane and out-of-plane $R_{AA}(p_T, \phi)$ depends on the chosen hydro model as can be seen from Fig. 5.5. Thus in principle the hydrodynamical medium can be probed with the hard partons, but currently the uncertainties related to the energy loss calculations are so large that no serious constraints can be presently put on the hydrodynamical models from jet-quenching.

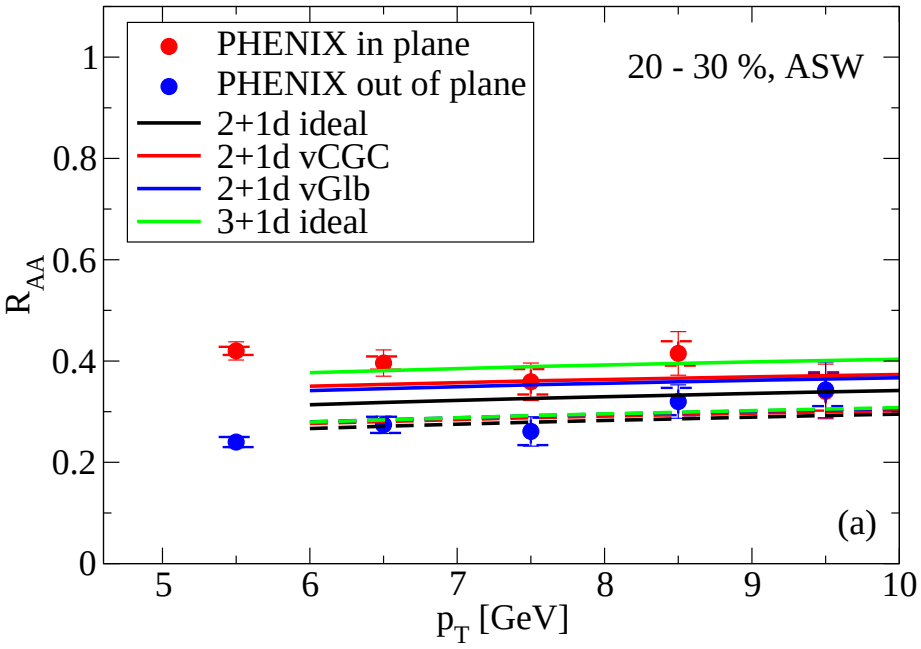

Figure 5.5: Nuclear suppression factor R_{AA} in 20-30% central Au+Au collisions at $\sqrt{s_{NN}}$ = 200 GeV with several hydrodynamical backgrounds. Data are from the PHENIX Collaboration [153]. From [II].

Chapter 6

Main results

In this chapter I summarize the main results of the articles included in this thesis. The main focus is on the event-by-event hydrodynamical results in Ref. [I] and on the thermal photon production in Refs. [III, V]. The interesting energy loss results presented in [II, IV] are, however, excluded from the discussion here since the author has not performed any of these R_{AA} calculations. First I will go through the obtained main results for the Au+Au collisions at $\sqrt{s_{NN}} = 200$ GeV and then I will move to the Pb+Pb collisions at $\sqrt{s_{NN}} = 2.76$ TeV.

All RHIC calculations discussed here use an initial time $\tau_0 = 0.17$ fm and the freeze-out temperature is $T_f = 160$ MeV with eosL and s95p and $T_f = 140$ MeV with eosQ. At the LHC the initial time is $\tau_0 = 0.12$ fm and the freeze-out temperatures are the same as in RHIC unless otherwise stated. Every calculation is performed without dissipative effects.

6.1 Event-by-event hydrodynamical simulations for RHIC

6.1.1 Hadron spectra

Let us first consider the effects of the event-by-event fluctuations to the hadronic variables as studied in Ref. [I]. In Fig. 6.1 I plot the transverse momentum spectra of positively charged pions, obtained from our event-by-event calculations with two different smearings σ and from the averaged smooth initial state. These calculations are initiated with the eWN profile from the MCG model as explained in Sec. 3.2. All calculations are close to the PHENIX data [156] below $p_T \approx 2$ GeV. At higher p_T, however, there are some deviations between the theory predictions. The event-by-event calculation with $\sigma = 0.4$ fm gives more high-p_T particles than the one with a larger fluctuation size or the calculation with an averaged initial

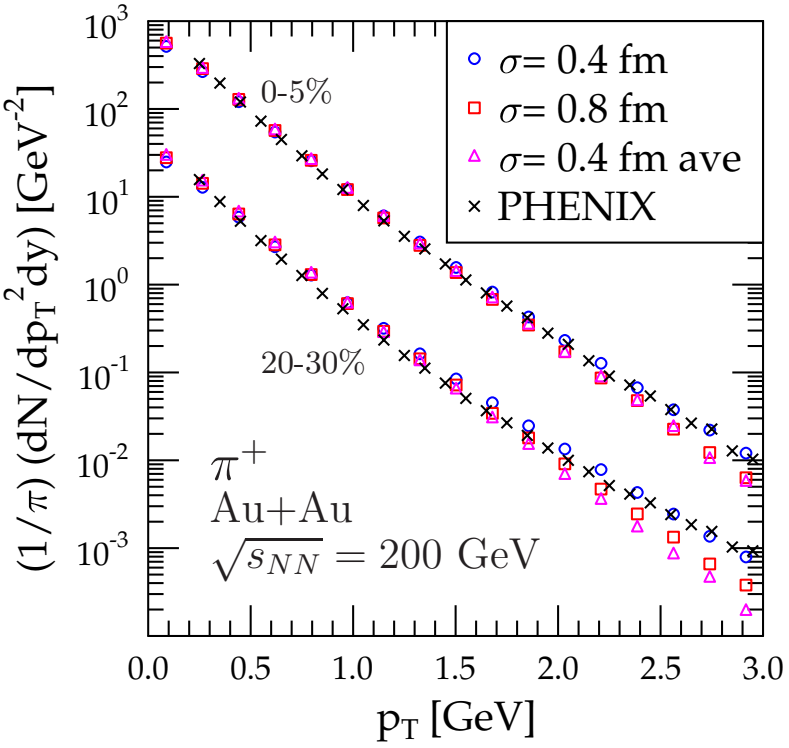

Figure 6.1: The transverse momentum spectra of positively charged pions in Au+Au collisions at $\sqrt{s_{NN}} = 200$ GeV. Event-by-event hydrodynamical calculations with two different smearing radii σ and the hydrodynamical calculation with averaged smooth initial conditions are presented. The experimental data are from the PHENIX Collaboration [156]. From [I].

state. This can be understood as follows: when the smearing radius σ is small, the pressure gradients in the initial state are larger, and more flow is generated. Thus the number of high-p_T particles is increased. However, when σ is sufficiently large, the pressure gradients do not differ much from the ones present in the smooth initial state and thus the p_T-spectra are similar in these cases. As was mentioned earlier in Sec. 3.2, the current MCG implementation causes the total entropy to vary as a function of σ. This can indeed be seen from Fig. 6.1 where the calculations with different σ deviate slightly from each other also in the low-p_T region, which determines the multiplicity. All in all, however, the agreement with the data is good enough and hence the elliptic flow can be meaningfully studied.

6.1.2 Elliptic flow

Figure 6.2 contains the main result of this thesis. In this figure we have plotted the elliptic flow of charged hadrons with different reference planes at various centralities. From the panel (a), where the most central collisions are considered, one sees that the calculation with the averaged initial state is clearly below the PHENIX [157, 158] and STAR [159] event plane data. Now looking at the event-by-event results this difference can be understood.

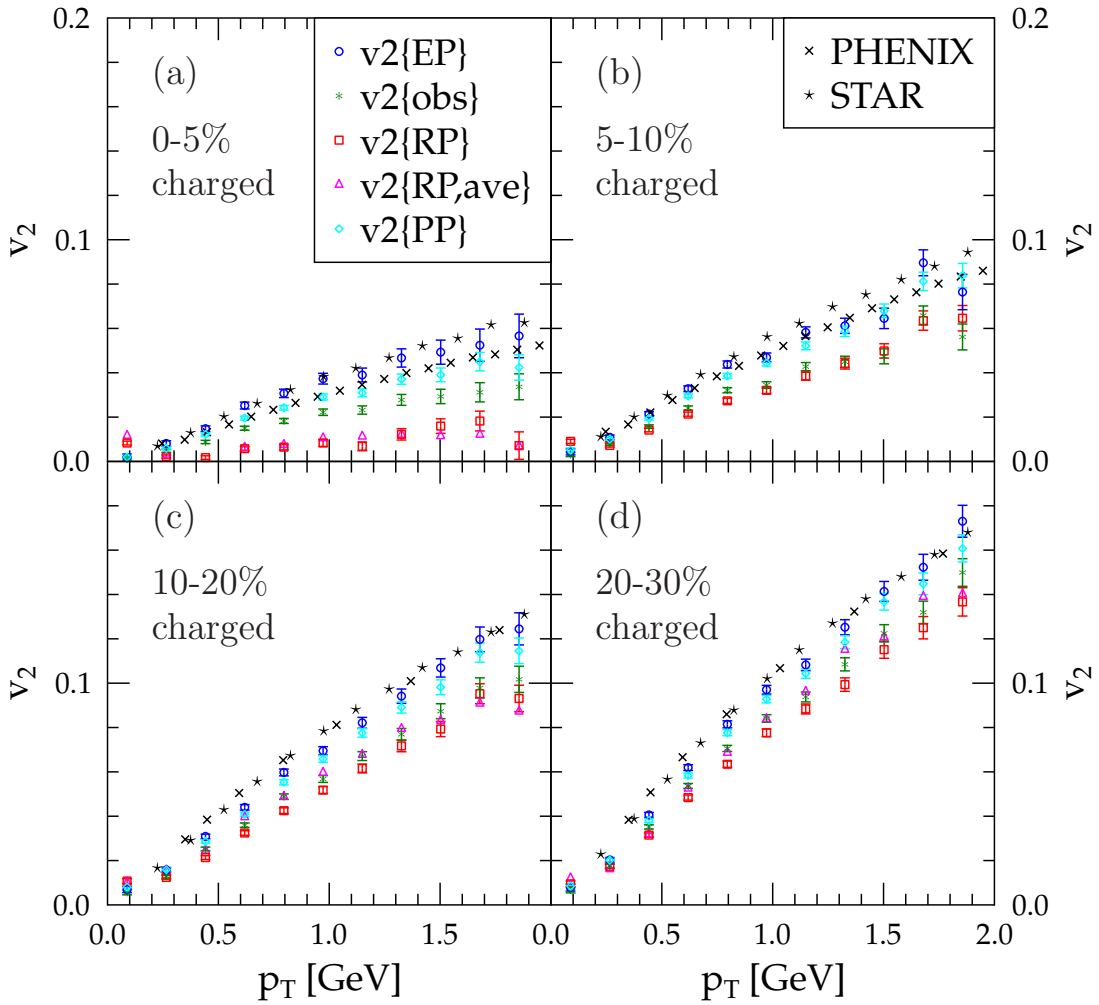

Figure 6.2: The elliptic flow of charged hadrons at different centralities in Au+Au collisions at $\sqrt{s_{NN}} = 200$ GeV. Event-by-event calculations with respect to different reference planes as well as the averaged initial state calculations are compared with $v_2\{\mathrm{EP}\}$ from the PHENIX [157, 158] and STAR [159] Collaborations. From [I].

The event-by-event v_2 results with respect to the RP are almost identical to the ones from the averaged initial state. This shows that the inclusion of the density fluctuations does not generate any v_2 as such. However, when the EP method is used, the computed $v_2\{\mathrm{EP}\}$ becomes clearly larger than $v_2\{\mathrm{RP}\}$ and $v_2\{\mathrm{RP,ave}\}$ especially in the most central collisions. Now the agreement with the experimental $v_2\{\mathrm{EP}\}$ data is remarkably good. This shows that the reference plane definition is vitally important in the v_2 analysis, and for making meaningful comparisons of theory and data.

Figure 6.2 shows also the unphysical $v_2\{\mathrm{obs}\}$. From here one can see that the difference between $v_2\{\mathrm{obs}\}$ and $v_2\{\mathrm{EP}\}$ decreases when moving towards peripheral collisions, meaning that $\mathcal{R}$ increases towards unity. This is also seen in the experiments [157–159] and if one considers very peripheral collisions, the difference would start to grow again since the number of the particles starts to be so small that an accurate determination of the event plane becomes more and more difficult. However, the hydrodynamical studies should not be extended to that peripheral collisions, where the validity of hydrodynamics starts to be questionable.

Finally, the elliptic flow with respect to the PP is considered. The obtained v_2s with respect to the EP and PP are very similar, but $v_2\{\mathrm{PP}\}$ is always slightly below $v_2\{\mathrm{PP}\}$. These results suggest that the PP is quite a good approximation for the EP.

Since the smearing radius σ is a free parameter in our event-by-event framework, the sensitivity of the elliptic flow to this parameter must be studied. In Fig. 6.3 I plot v_2 with respect to the RP and EP using two different smearing radii. In both centrality classes shown in the figure the obtained elliptic flow does not depend on the σ parameter. Thus with the current MCG implementation, the multiplicity and p_T-spectra are sensitive to the smearing parameter σ, but elliptic flow is not.

The correlation between the event plane and the participant plane is further studied in Fig. 6.4 where the distributions of the angle differences between EP (ψ_2 in Eq. (4.3)) and PP (ψ_{PP} in Eq. (3.25)) are plotted. Also the angle difference between EP and RP (ψ_{RP} is in the direction of the impact parameter) is considered. From this it can be seen that the peaks around $\psi_{\mathrm{EP}} \approx \psi_{\mathrm{PP/RP}}$ are narrower with the PP than with the RP. This indicates that the EP is closer to the PP, as suggested by the v_2 results. The fluctuations around the true event plane are included in here and they widen the peaks. Based on the observations made here, one can indeed consider PP as quite a good approximation for the EP. This correlation is observed also with the higher harmonics [61, 65].

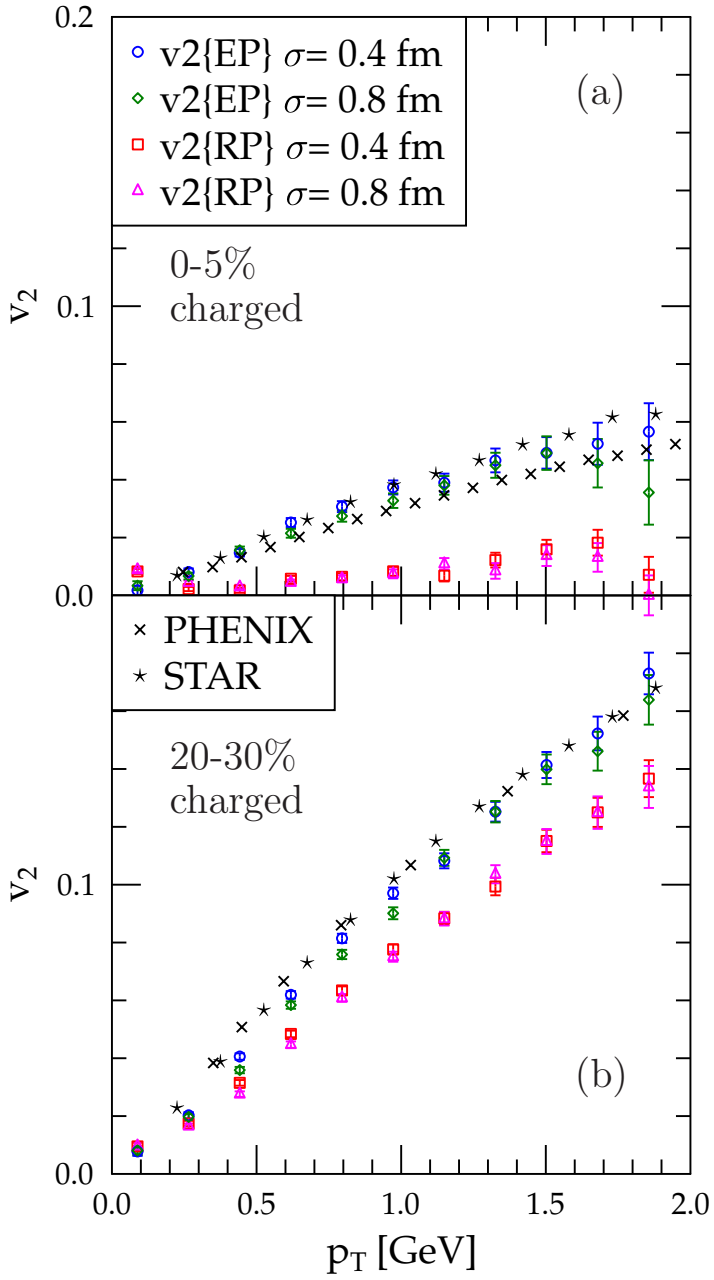

Figure 6.3: A comparison between charged hadron elliptic flow results with different fluctuation size parameters σ. Data from the PHENIX [157, 158] and STAR [159] Collaborations. From [I].

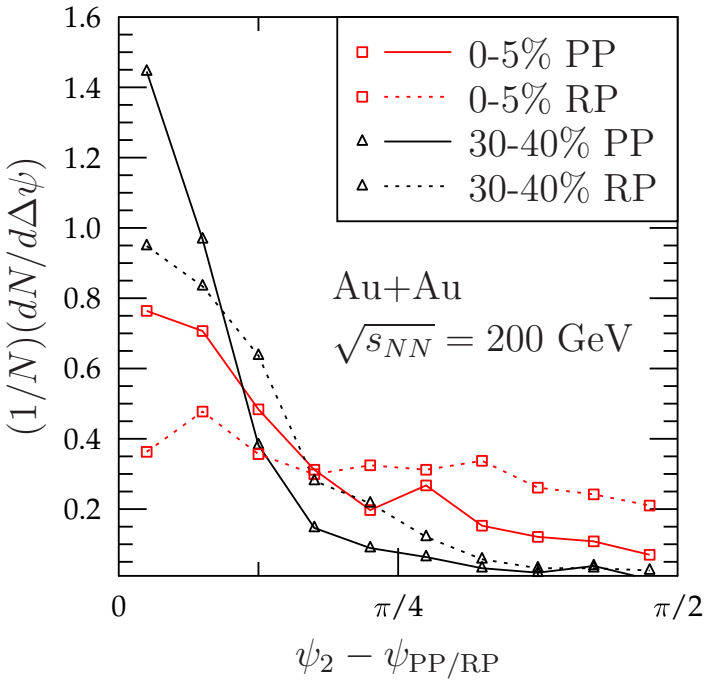

Figure 6.4: The distributions for the angle differences $\Delta\psi = \psi_2 - \psi_{\mathrm{PP/RP}}$ at two centralities in Au+Au collisions at $\sqrt{s_{NN}} = 200$ GeV. From [I].

6.1.3 Triangular flow

Finally the higher harmonic, triangular flow v_3, is calculated and compared with the data in Fig. 6.5. Here it is not meaningful to calculate the triangular flow with respect to the RP, since v_3 is entirely due to fluctuations and there are no preferred directions solely due to the impact parameter, and thus $v_3\{\mathrm{RP}\}$ is simply zero. The v_3 measured by the PHENIX Collaboration [160] very recently is generally below the prediction from our event-by-event hydrodynamical model. As has been shown in Refs. [63, 106], the triangular flow should be more sensitive to the shear viscosity than the elliptic flow. Thus the initial state used here should be tuned so that more v_2 is obtained and then after the viscous damping, both v_2 and v_3 should match the data. In Ref. [63] it was shown that for example with a bit of BC component added to the initial state and with $\eta/s = 0.08$ in the viscous hydrodynamics, one can arrive at a good agreement with both v_2 and v_3.

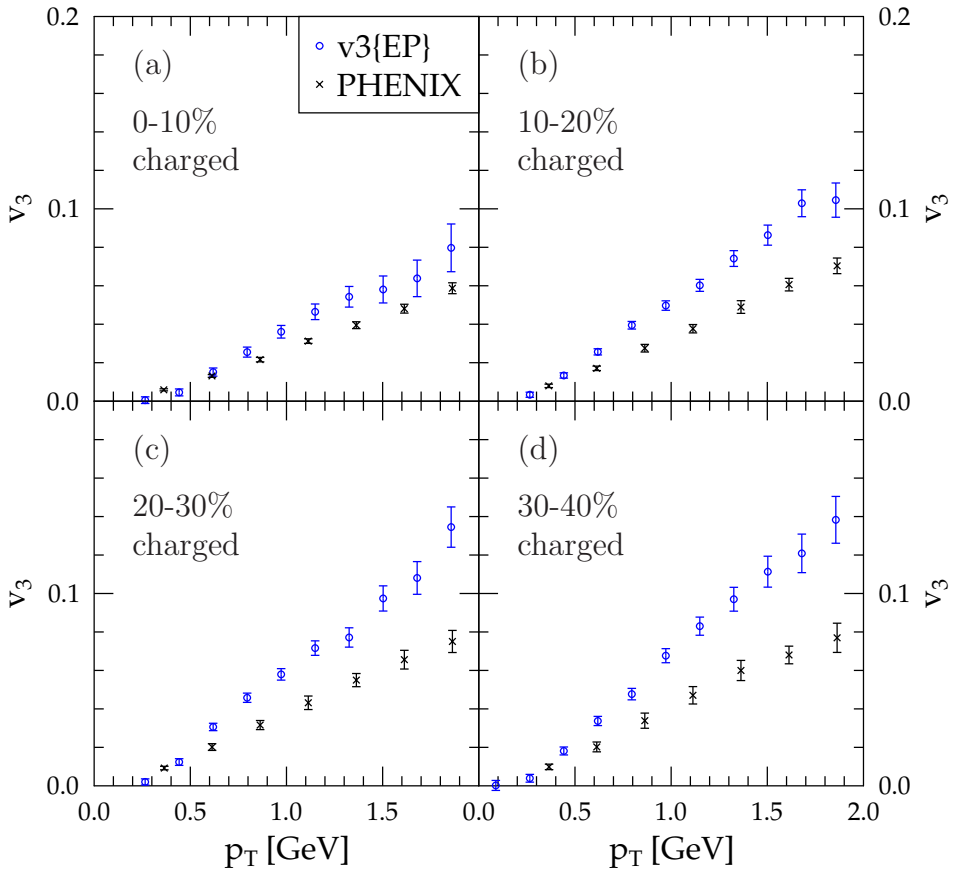

Figure 6.5: Triangular flow of charged hadrons in Au+Au collisions at $\sqrt{s_{NN}}$ = 200 GeV. Data are from the PHENIX Collaboration [160].

6.2 Thermal photons at RHIC

Next, I consider the thermal photons and especially their elliptic flow. Here I concentrate on the photon emission calculations done with the smooth optical Glauber profiles in Ref. [V]. The event-by-event results for the photon p_T-spectra from Ref. [III] are shown in Sec. 6.3.

Figure 6.6 shows the thermal photon p_T-spectra, experimental data and the fits from Sec. 5.3. These calculations have been performed with the sWN initial transverse profile, which is obtained from the optical Glauber model. The difference between the fits (total yields) and the thermal photon calculations is smallest around $p_T \sim 2.5$ GeV and most likely near this transverse momentum there exists a p_T-window, where the photon production is dominated by the thermal emission. In the low-p_T region the thermal calculations are well below the data. This is

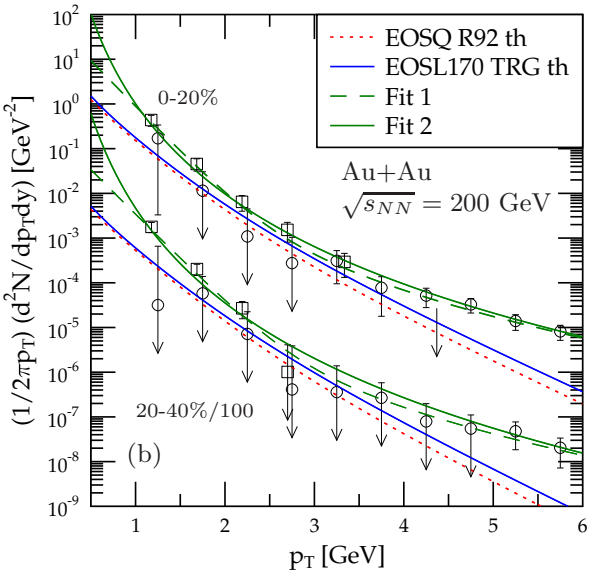

Figure 6.6: The transverse momentum spectra of direct photons in Au+Au collisions at $\sqrt{s_{NN}} = 200$ GeV from the thermal photon calculations and fits presented in Sec. 5.3. Data are from the PHENIX Collaboration [138, 139]. From [V].

a common feature in almost all of the current thermal photon calculations [161]. However, for example in Ref. [162], where also additional $2 \rightarrow 3$ processes are included in the HG photon rate calculation, the agreement with the data is better. Also the baryonic contributions can be important in this region [126, 163].

The thermal photon calculations shown in Fig. 6.6 differ roughly by a factor of two in the high-p_T region. This is mostly due to the slightly different mapping of the energy density to the temperature in the EoSs. The difference is not large, but the exponential temperature dependence in the emission rates magnifies the effect. In both cases the plasma emission dominates almost always. When the TRG rates and eosL are used, only 3% of the photons come from the HG at $p_T = 1$ GeV. With eosQ and the R92 rates about 50% of the photons originate from the HG at the same p_T. In both cases this fraction decreases very quickly when moving towards higher p_T.

Thermal photon elliptic flow is plotted in Fig. 6.7. Calculations with the R92 rates are shown in panel (a) and the ones with TRG rates in panel (b). The largest v_2 is obtained with the eosQ and R92 rates. With the eosQ the mixed and HG phases are long-lived and since the R92 rate is larger than TRG, the amount of photons from the HG is largest in this case. Since the flow anisotropy is large in

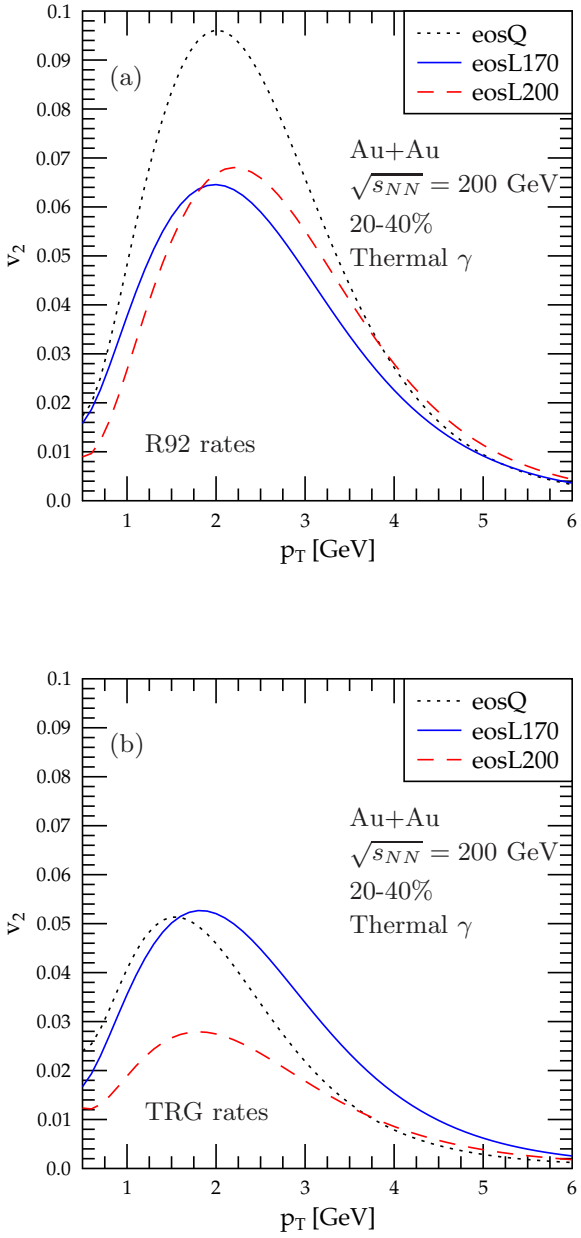

Figure 6.7: Elliptic flow of thermal photons in Au+Au collisions at $\sqrt{s_{NN}} = 200$ GeV. In panel (a) the R92 rates for HG are used and the calculations shown in panel (b) are performed with the TRG rates. From [V].

the HG phase, the largest photon v_2 is obtained when the amount of photons from the HG is largest.

From panel (a) one also sees that the switching temperature T_s has only a minor effect in the v_2 obtained with the R92 rates. This is due to the fact that the emission rates for the QGP and HG are quite similar at the most relevant E region as was shown in Fig. 5.3. However, in panel (b) the situation is very different. The larger switching temperature leads to much smaller elliptic flow. Again from Fig. 5.3 one sees that the TRG rate and the QGP rate are quite different and thus the overall emission from the temperature region $T = 170 - 200$ MeV is decreased when the T_s is increased. These temperatures give a large contribution to the v_2 value since the flow has already developed and temperature is still quite high. Thus the amount of large-v_2 photons is decreased relative to the small-v_2 photons and hence the total elliptic flow becomes smaller.

Our predictions for the total direct photon v_2 together with the thermal photon v_2 are presented in Fig. 6.8. The direct photon elliptic flow is obtained from Eq. (5.2) and the total photon yield is from the Fit 1. From this figure one sees that the other components – if they indeed are of non-thermal nature and nearly isotropic – can wash away a significant amount of the thermal photon v_2. Thus it is important to compare the photon p_T-spectra simultaneously with the elliptic flow. Also the difference between the eosQ and eosL results is smaller in the direct photon case than in the thermal one. This is due to the fact that with the eosQ more production from the other components is needed to match the measured photon spectra and thus the elliptic flow is affected more by the other components.

The direct photon v_2 results are compared against the very recent PHENIX data [135] in Fig. 6.9. Very interestingly, the data is clearly above the predictions presented in Ref. [V], even above the eosQ thermal photon case. Only the 20-40% centrality class is considered here since in central collisions part of the difference should come from the fact the PHENIX has measured the photon v_2 with respect to the event plane determined from the hadrons, while we compute the photon $v_2\{\mathrm{RP}\}$. However, in the 20-40% centrality class the difference between the EP and RP results should be reasonably small, since the situation is most likely very similar to the hadronic case.

To get such a large v_2, one possibility is that the photon emission from the HG must be larger than what we have estimated. It is possible that the rates are still too small, or that the HG phase is too small since in order to reproduce the hadronic p_T-spectra, we decouple the system at a relatively high T_f. By introducing a partial chemical equilibrium [164] in the EoS, the system lifetime could be increased [165], in which case the HG emission would grow also. Then, however, the chemical potentials introduced by the chemical freeze-out should be taken into account in the rate calculations.

To test how much more thermal photon v_2 would be obtained with a lower T_f

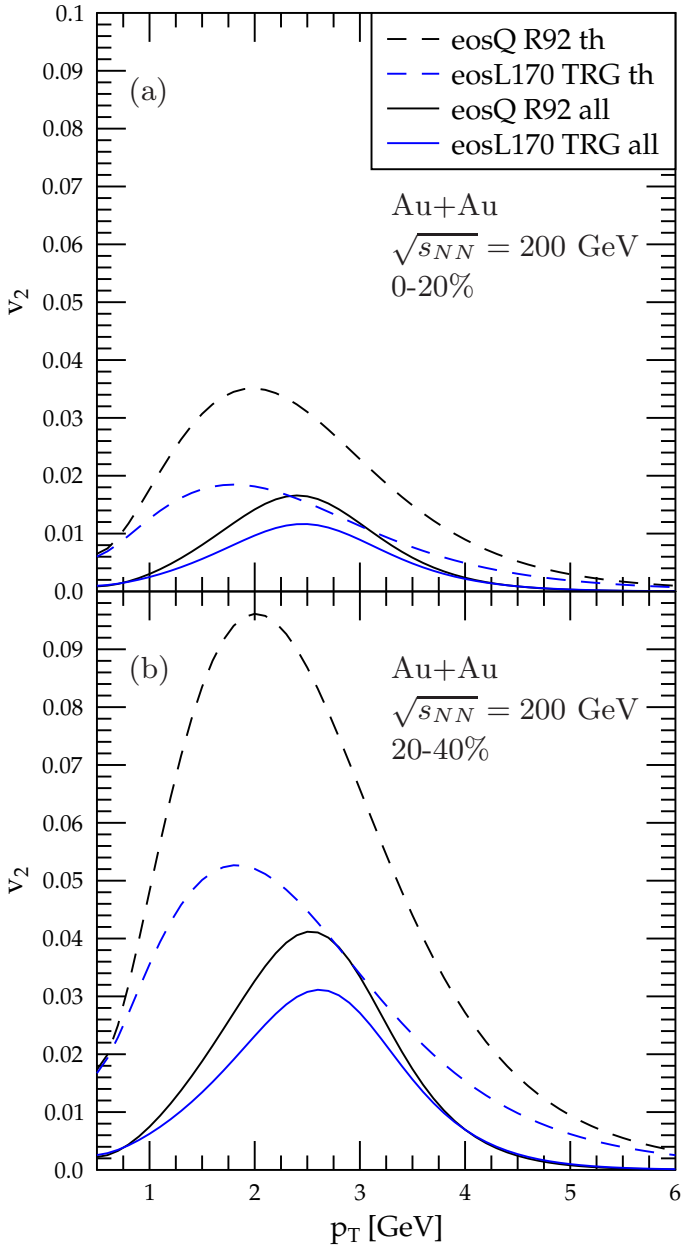

Figure 6.8: Elliptic flow of thermal and direct photons in Au+Au collisions at $\sqrt{s_{NN}}$ = 200 GeV. The total photon yield used in direct photon v_2 estimate is from Fit 1. From [V].

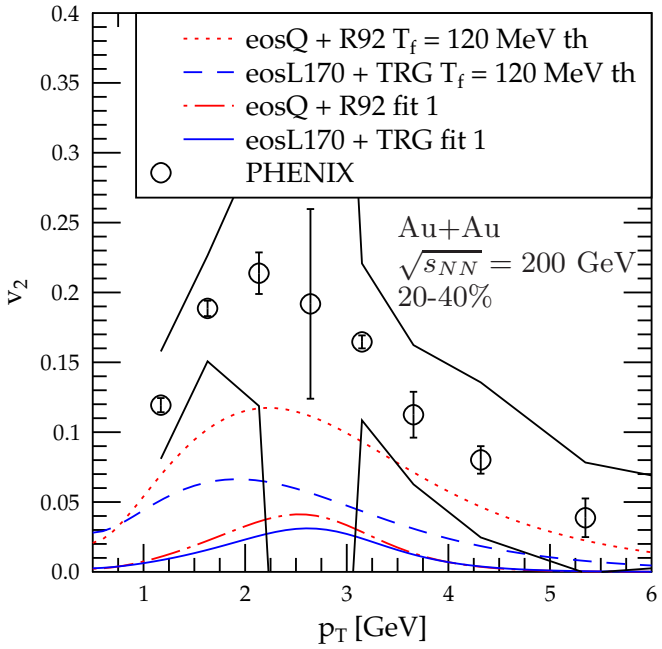

Figure 6.9: Elliptic flow of thermal and direct photons from hydrodynamical calculations compared with $v_2\{\mathrm{EP}\}$ measurements from the PHENIX Collaboration [135] in 20-40% central Au+Au collisions at $\sqrt{s_{NN}} = 200$ GeV.

(and ignoring the resulting mismatch between the obtained hadronic p_T-spectra and data) I have repeated the calculation also with $T_f = 120$ MeV, and shown the results in Fig. 6.9. The eosQ + R92 result can be considered as an upper limit for the v_2 that can be obtained from the current model. With the eosQ the v_2 is close to the lower limit of the data, but with the eosL170 the obtained v_2 is still far away from the data even in this extreme case. We thus conclude that the measured photon v_2 cannot be explained with the current model. But the good news is that this large v_2 should be possible only if the thermal emission is the dominant contribution in the few GeV p_T-region.

6.3 Thermal photons from event-by-event hydrodynamics at RHIC

The effects of the initial density fluctuations in the thermal photon p_T-spectra are considered in Fig. 6.10. In this study [III] the sWN profile from the MCG model

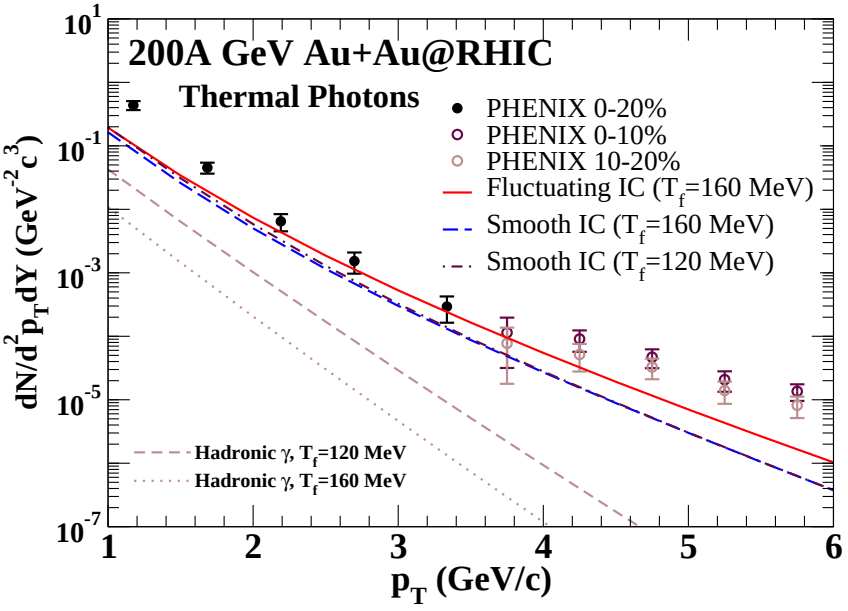

Figure 6.10: The transverse momentum distribution of thermal photons from event-by-event and smooth hydrodynamical calculations. Hadronic contributions with two different freeze-out temperatures are also shown. Data are from the PHENIX Collaboration [138, 139]. From [III].

is used for the initial conditions. A large increase of thermal photon production at the intermediate p_T is observed when the size parameter $\sigma = 0.4$ fm is used. The hot spots, which are present in the event-by-event calculations, cause a strong enhancement in the thermal photon emission since the rates have an exponential temperature dependence. As mentioned before, the fluctuations also increase the transverse flow in the system and thus the effect of the flow boosts shown in Fig. 5.1 becomes larger. However, the flow affects mostly the HG emission and since the spectra are dominated by the QGP emission, the increased transverse flow cannot be seen in the total p_T-spectrum.

Also in here the sensitivity of the spectra to the fluctuation size parameter σ is studied. Figure 6.11 shows the ratio of the photon yield at several values of p_T as a function of σ. The difference between the event-by-event calculation and the averaged initial state calculation decreases when σ increases. The same phenomenon was observed with the hadrons in Fig. 6.1 but for a different reason. In the photon case the increasing smearing radius decreases the temperature of the hot spots and thus emitted photon yield becomes smaller. The effect is larger for high-p_T photons since these are dominated by the very high temperature emission.

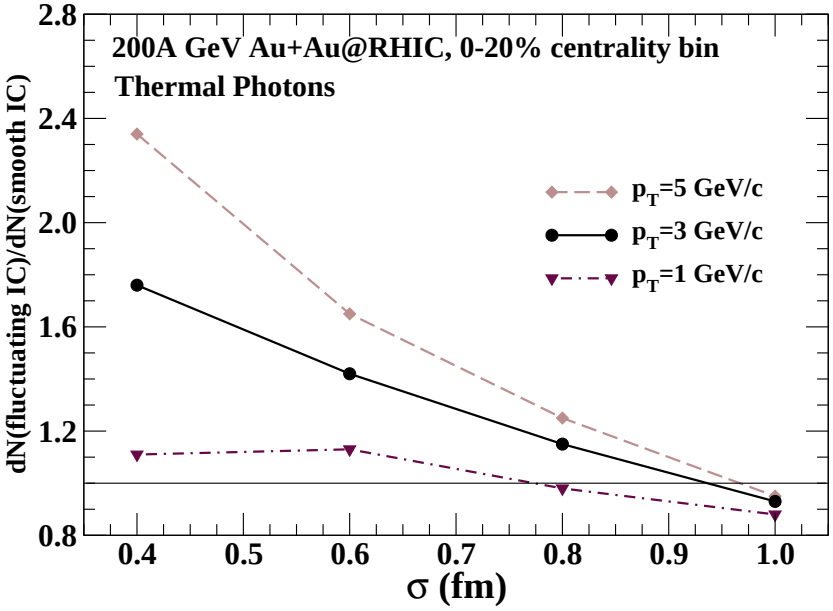

Figure 6.11: The ratio of the photon spectra with and without the initial density fluctuations as a function of the fluctuation size parameter in central Au+Au collisions at $\sqrt{s_{NN}} = 200$ GeV.

6.4 LHC results: hadron p_T-spectra and thermal photons

Finally I will present our recent LHC results for the hadron p_T-spectra and predictions for the thermal photons. In Ref. [IV] we considered the LHC initial state from the viewpoint of the EKRT model. The original multiplicity prediction by the model was a little, $\mathcal{O}(10\%)$, too high in comparison with the first LHC data [99, 166], and the next-to-leading order pQCD analysis has not yet been completed with the updated parton distribution functions [165]. Therefore, in Ref. [IV], an EKRT-motivated fit was made. The idea was to fix the K-factor in the pQCD mini-jet calculation in such a way that the measured LHC total multiplicity [166] is reproduced with $\sigma\langle E_T\rangle$ and τ_0 taken from the EKRT model, and with the freeze-out temperature T_f fixed at RHIC. The transverse density profile is eBC from the optical Glauber model and $T_f = 165$ MeV. The fit gives $K = 1.54$ and in this case the initial time is $\tau_0 = 0.12$ fm.

In Fig. 6.12 the uncertainties in the fit and in the hydro parameters have been charted. From panel (a) one can see that a later freeze-out temperature is not favored by the ALICE data [140]. As discussed in Sec. 3.6, the initial time does

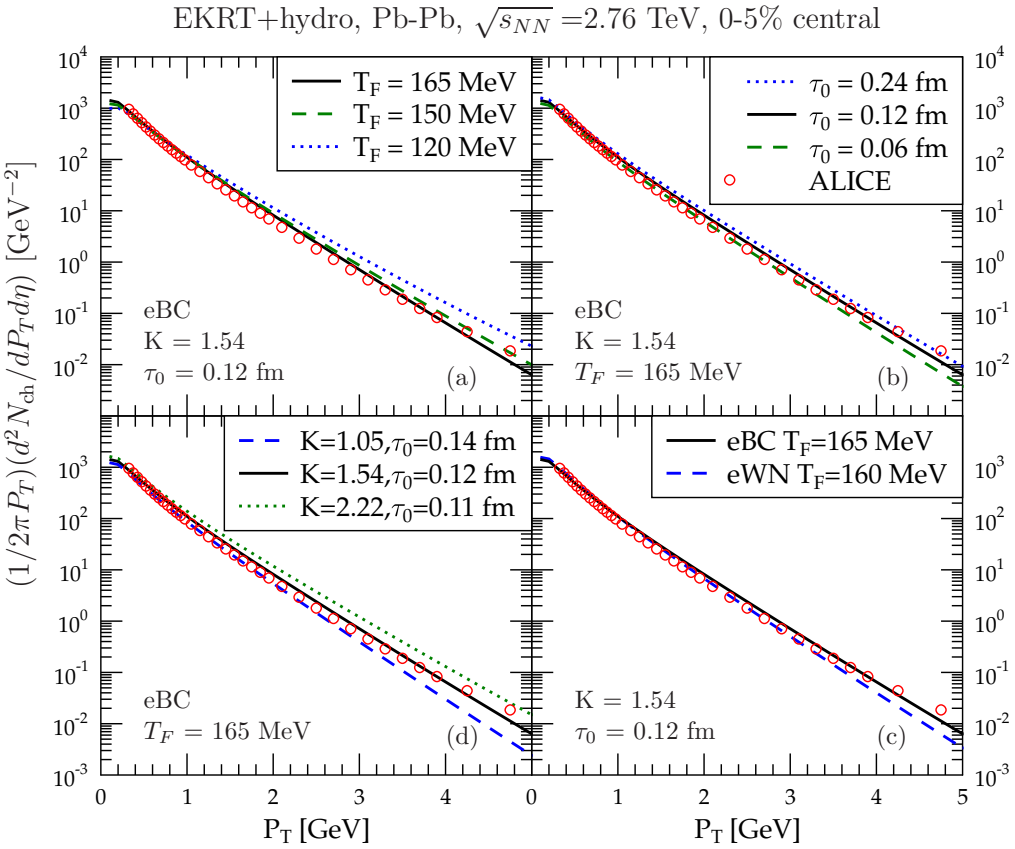

Figure 6.12: The transverse momentum spectra of charged hadrons in central Pb+Pb collisions at $\sqrt{s_{NN}}$ = 2.76 TeV. Dependence of the different parameters are charted. Data from the ALICE Collaboration [140]. From [IV].

not need to be exactly $\tau_0 = 1/p_{\rm sat}$ as given by the EKRT model, but $\tau_0 \propto 1/p_{\rm sat}$. In panel (b) the initial time is varied by a factor of two. The larger initial time is now disfavored by the data and, perhaps surprisingly, also a smaller τ_0 gives a good agreement with the data. In here the computed $\sigma\langle E_T\rangle$ is kept constant and thus the multiplicity depends on τ_0 as explained in Ref. [IV].

In the (c) panel the transverse profile is switched to the eWN and the freeze-out temperature has been fixed so that at RHIC the pion spectrum in central collisions [156] is well reproduced. Here the region $2-3$ GeV favors the eWN profile but above 3 GeV the eBC is closer to the data. Finally in panel (d) we have plotted the sensitivity to the fit parameter K. Since the K factor affects the value of the saturation scale, also the initial time changes when the K factor is varied. Here the $K = 1.54$ case reproduces the LHC multiplicity best while the two other cases

give $\sim 20\%$ too small or large multiplicity.

From Fig. 6.12 we conclude that in our framework the possible variations of K, τ_0 and T_f around the default values are fairly well constrained. However, the uncertainty in the initial transverse profile is large. The fine-tuning of the initial state model is left for future work, where the centrality dependence of the p_T-spectra as well as v_2 will be considered.

Next, let me discuss our predictions for the thermal photon production at the LHC. Here the initial profile is taken to be the sWN from the optical Glauber model. Figure 6.13 shows thermal photon p_T-spectra in Pb+Pb collisions at $\sqrt{s_{NN}} = 2.76$ TeV. The two cases that produce the largest and smallest yield, eosL170 + R92 and eosQ + TRG, are picked from all the possibilities considered in this thesis and Ref. [V]. All other cases we studied go in the shaded areas.

Finally in Fig. 6.14 I have plotted our thermal photon elliptic flow prediction for the Pb+Pb collisions at the LHC. In this case the measured photon spectra are not known yet and thus we cannot estimate how much v_2 might be washed away by the photon production from the other components without additional theoretical predictions for the other components. If this figure is compared with Fig. 6.7 one

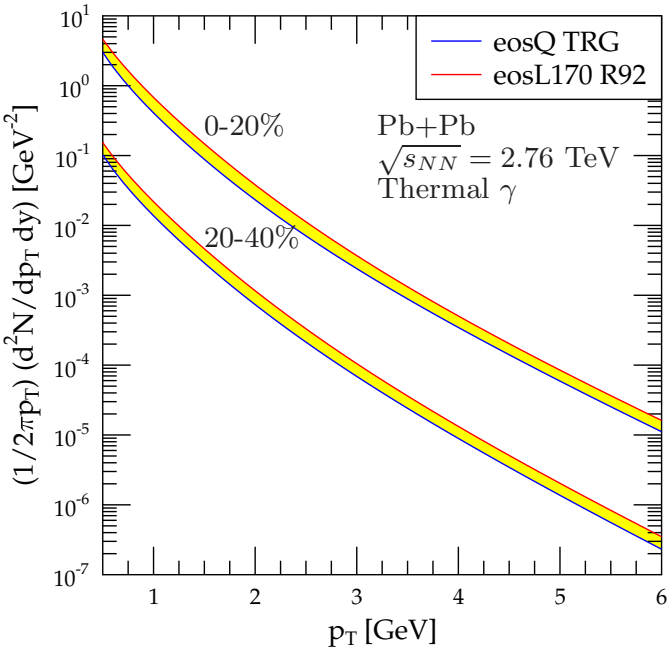

Figure 6.13: Prediction for the thermal photon transverse momentum spectra the Pb+Pb collisions at $\sqrt{s_{NN}} = 2.76$ TeV. From [V].

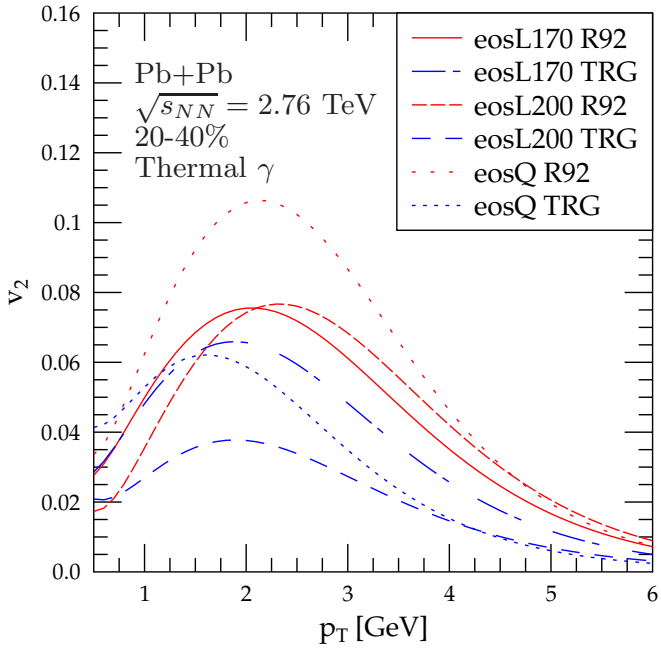

Figure 6.14: Predictions for the thermal photon elliptic flow for 20-40% central Pb+Pb collisions at $\sqrt{s_{NN}} = 2.76$ TeV. From [V].

can see that the obtained elliptic flow is surprisingly similar at RHIC and LHC, although the evolution and volume of the plasma is quite different in these cases. However, since the other photon production mechanisms may play a role in v_2, and especially since the latest RHIC photon v_2 data are not yet understood, these predictions have fairly large uncertainties.

Chapter 7

Conclusions and outlook

The event-by-event hydrodynamical calculations presented here show the importance of the initial state density fluctuations. By taking the initial state average while rotating each event appropriately also higher order flow coefficients v_n ($n \geq 2$) can be studied one at the time with smooth hydrodynamics [106], but genuine event-by-event calculations are needed to study all of the coefficients at once.

As can be seen from our elliptic flow results, the definition of the reference plane in the elliptic flow analysis is very important. In this thesis only the event plane method was used to calculate v_2 and v_3. In the future also other flow analysis methods should be used. Since these methods depend on the flow fluctuations and the non-flow differently, a one-to-one comparison with the experiments should be made using several flow analysis methods.

Recently lots of flow coefficient data have been published and harmonics up to $n = 6$ have been measured [105]. Most of the hydrodynamical calculations have concentrated only on the elliptic and triangular flow, but more studies about higher harmonics should be made. Hydrodynamical calculations however need to be run on a very fine grid in order to produce the higher coefficients reliably [38]. However, with the modern computer resources this problem should be tackled in the near future.

The viscous effects should not be forgotten and the same calculations presented in here should be repeated with viscous event-by-event hydrodynamics. As already seen in this thesis, the elliptic and triangular flow cannot be simultaneously fitted with ideal hydrodynamics. Flow coefficients (mostly v_2) have been used to estimate the value of the shear viscosity and thus it is vitally important to understand the effects of the initial state fluctuations before extracting the shear viscosity from the RHIC and LHC data. Also here the higher flow coefficients can be expected to be important since the viscous effects are larger for higher harmonics.

All of the calculations presented in this thesis assumed longitudinal boost in-

variance. Beyond the mid-rapidites for example the hadron spectra and v_2 at RHIC have a rapidity dependence [167] and a full 3+1-dimensional hydrodynamical code is needed before this behavior can be studied. When the assumption of the boost-invariance is relaxed, the initial conditions are needed also for the longitudinal direction. Naturally the ultimate goal in the future is to develop a 3+1-dimensional event-by-event viscous hydrodynamical code. Schenke et. al [63] have already developed such a code, but it would be very important to test two independently developed codes against each other.

The freeze-out procedure applied in this thesis is a simple and convenient approach and there may be more proper ways to handle the late time evolution and the freeze-out. Since with the fluctuations the flow develops very irregularly, one should study in more detail whether the constant temperature freeze-out is reasonable. Posing a dynamical freeze-out condition similar to the one used in Ref. [46] would be very interesting especially in the event-by-event context. Also using a hadron cascade as an afterburner [37, 47–53] would be an option. However there are still considerable uncertainties on how the cascade should be matched with hydrodynamics. One big question is whether there exists a region where both approaches give the same physics. If such a region exists, switching from one model to another can be made safely. If this region does not exist, then one has to think whether the switching can be made at all.

The direct photons are expected to be an important probe for the QGP evolution. Thermal and jet-medium photon calculations need a good understanding of the underlying medium. Thus the photon measurements in the low and intermediate p_T-region, where the production mechanisms mentioned above dominate, could be utilized to constrain the medium parameters as well as the uncertainties in the theory calculations. It is, however, possible that there is too much freedom in the model parameters and the photon data alone cannot be used to put rigorous enough constraints. In this case a multi-observable approach is needed.

The direct photon v_2 measured by PHENIX very recently was much higher than expected from any of the existing thermal photon calculations [92, 118, 119, V]. Thus there is now much work to do before the measurement is well understood. Naturally the event-by-event density fluctuations can be important for the photon v_2. At least in the thermal photon spectra we saw a very large effect and first v_2 calculations are presented in [168]. Also the viscous effects should be taken into account in the photon calculations, but there the situation is more complicated since the emission rates must also be recomputed by including the viscous corrections [168, 169]. In this situation it is very interesting to see what the photon v_2 will be at the LHC.

The long-awaited LHC era has now begun, and the first results obtained from the Pb+Pb collisions have not offered a big surprise from the hydrodynamical point of view: this suggests that we are on the right track in describing the QCD matter

as a nearly ideal fluid. In addition to the highest-energy RHIC data, the RHIC energy scan has produced flow data at lower energies [170]. Thus the situation is now very good since lots of new exiting flow measurements from the RHIC and the LHC experiments are available. A combined systematic analysis of the flow data at different energies and system sizes (Au+Au and Cu+Cu at RHIC) would help to constrain the initial state of the produced QCD matter as well as its viscosity.

Appendix A

List of acronyms

ALICE	A Large Ion Collider Experiment
ASW	Energy loss formalism introduced in Ref. [143]
BC	Binary Collisions
BNL	Brookhaven National Laboratory
CERN	European Laboratory for Particle Physics
CGC	Color Glass Condensate
CM	Center of Mass
CPU	Central Processing Unit
eBC	Initial state where the energy density is distributed according to the binary collision density
EKRT	Initial state model introduced in Ref. [23]
EoS	Equation of State
eosL	QCD-matter equation of state from Ref. [44]
eosL170	eosL where the switching temperature $T_s = 170$ MeV is used in the thermal photon calculation
eosL200	eosL where the switching temperature $T_s = 200$ MeV is used in the thermal photon calculation
eosQ	QCD-matter equation of state from Ref. [43]
EP	Event Plane
eWN	Initial state where the energy density is distributed according to the wounded nucleon density
HG	Hadron Gas
IC	Initial Conditions
IS	Israel and Stewart, see Ref. [74]
LHC	Large Hadron Collider
LO	Leading Order
LYZ	Lee-Yang Zeros
MCG	Monte Carlo Glauber

NLO	Next-to-Leading Order
PDF	Parton Distribution Function
PHENIX	Pioneering High Energy Nuclear Interaction eXperiment
PP	Participant Plane
pQCD	Perturbative Quantum ChromoDynamics
PYTHIA	Event generator introduced in Ref. [70]
QCD	Quantum ChromoDynamics
QGP	Quark-Gluon Plasma
R92	Photon emission rates from Refs. [123–125]
RHIC	Relativistic Heavy-Ion Collider
RP	Reaction Plane
s95p	QCD-matter equation of state from Ref. [21]
sBC	Initial state where the entropy density is distributed according to the binary collision density
SHASTA	SHArp and Smooth Transport Algorithm [40, 41]
SPS	Super Proton Synchrotron
STAR	Solenoidal Tracker At RHIC
sWN	Initial state where the entropy density is distributed according to the wounded nucleon density
TRG	Photon emission rates from Ref. [126]
URHIC	UltraRelativistic Heavy-Ion Collisions
WN	Wounded Nucleon
W-S	Woods-Saxon

Bibliography

[I] H. Holopainen, H. Niemi, K. J. Eskola, Phys. Rev. **C83** (2011) 034901, arXiv:1007.0368 [hep-ph].

[II] T. Renk, H. Holopainen, U. Heinz, C. Shen, Phys. Rev. **C83** (2011) 014910, arXiv:1010.1635 [hep-ph].

[III] R. Chatterjee, H. Holopainen, T. Renk, K. J. Eskola, Phys. Rev. **C83** (2011) 054908, arXiv:1102.4706 [hep-ph].

[IV] T. Renk, H. Holopainen, R. Paatelainen, K. J. Eskola, arXiv:1103.5308 [hep-ph].

[V] H. Holopainen, S. S. Räsänen, K. J. Eskola, arXiv:1104.5371 [hep-ph].

[1] K. Nakamura *et al.* (Particle Data Group Collaboration), J. Phys. **G37** (2010) 075021.

[2] N. Cabibbo, G. Parisi, Phys. Lett. **B59** (1975) 67-69.

[3] J. C. Collins, M. J. Perry, Phys. Rev. Lett. **34** (1975) 1353.

[4] S. Borsanyi *et al.* (Wuppertal-Budapest Collaboration), JHEP **1009** (2010) 073, arXiv:1005.3508 [hep-lat].

[5] S. Mukherjee, *Quark Matter 2011 proceedings*, arXiv:1107.0765 [nucl-th].

[6] K. Adcox *et al.* (PHENIX Collaboration), Nucl. Phys. **A757** (2005) 184, arXiv:nucl-ex/0410003.

[7] J. Adams *et al.* (STAR Collaboration), Nucl. Phys. **A757** (2005) 102, arXiv:nucl-ex/0501009.

[8] B. B. Back *et al.*, Nucl. Phys. **A757** (2005) 28, arXiv:nucl-ex/0410022.

[9] I. Arsene *et al.* (BRAHMS Collaboration), Nucl. Phys. **A757** (2005) 1, arXiv:nucl-ex/0410020.

[10] K. Geiger, B. Muller, Nucl. Phys. **B369** (1992) 600-654.

[11] D. Molnar, M. Gyulassy, Phys. Rev. **C62** (2000) 054907, arXiv:nucl-th/0005051.

[12] Z. Xu, C. Greiner, Phys. Rev. **C71** (2005) 064901, arXiv:hep-ph/0406278.

[13] Z. Xu, C. Greiner, Phys. Rev. **C76** (2007) 024911, arXiv:hep-ph/0703233.

[14] J. D. Bjorken, Phys. Rev. **D27** (1983) 140-151.

[15] K. Kajantie, L. D. McLerran, Phys. Lett. **B119** (1982) 203.

[16] K. Kajantie, L. D. McLerran, Nucl. Phys. **B214** (1983) 261.

[17] K. Kajantie, R. Raitio, P. V. Ruuskanen, Nucl. Phys. **B222** (1983) 152.

[18] G. Baym, B. L. Friman, J. P. Blaizot, M. Soyeur, W. Czyz, Nucl. Phys. **A407** (1983) 541-570.

[19] H. Von Gersdorff, L. D. McLerran, M. Kataja, P. V. Ruuskanen, Phys. Rev. **D34** (1986) 794.

[20] L. D. McLerran, M. Kataja, P. V. Ruuskanen, H. von Gersdorff, Phys. Rev. **D34** (1986) 2755.

[21] P. Huovinen, P. Petreczky, Nucl. Phys. **A837** (2010) 26-53, arXiv:0912.2541 [hep-ph].

[22] S. Borsanyi, G. Endrodi, Z. Fodor, A. Jakovac, S. D. Katz, S. Krieg, C. Ratti, K. K. Szabo, JHEP **1011** (2010) 077, arXiv:1007.2580 [hep-lat].

[23] K. J. Eskola, K. Kajantie, P. V. Ruuskanen, K. Tuominen, Nucl. Phys. **B570** (2000) 379-389, arXiv:hep-ph/9909456.

[24] T. Lappi, R. Venugopalan, Phys. Rev. **C74** (2006) 054905, arXiv:nucl-th/0609021.

[25] H.-J. Drescher, Y. Nara, Phys. Rev. **C75** (2007) 034905, arXiv:nucl-th/0611017.

[26] H.-J. Drescher, Y. Nara, Phys. Rev. **C76** (2007) 041903, arXiv:0707.0249 [nucl-th].

[27] P. Romatschke, U. Romatschke, Phys. Rev. Lett. **99** (2007) 172301, arXiv:0706.1522 [nucl-th].

[28] M. Luzum, P. Romatschke, Phys. Rev. **C78** (2008) 034915, arXiv:0804.4015 [nucl-th].

[29] H. Song, U. W. Heinz, Phys. Rev. **C78** (2008) 024902, arXiv:0805.1756 [nucl-th].

[30] U. W. Heinz, J. S. Moreland, H. Song, Phys. Rev. **C80** (2009) 061901, arXiv:0908.2617 [nucl-th].

[31] H. Song, S. A. Bass, U. W. Heinz, T. Hirano, C. Shen, Phys. Rev. Lett. **106** (2011) 192301, arXiv:1011.2783 [nucl-th].

[32] K. Adcox *et al.* (PHENIX Collaboration), Phys. Rev. Lett. **88** (2002) 022301, arXiv:nucl-ex/0109003.

[33] C. Adler *et al.* (STAR Collaboration), Phys. Rev. Lett. **89** (2002) 202301, arXiv:nucl-ex/0206011.

[34] L. D. Landau and E. M. Lifshitz, "Fluid mechanics" Pergamon, Oxford, (1963).

[35] C. E. Aguiar, T. Kodama, T. Osada, Y. Hama, J. Phys. **G27** (2001) 75-94, arXiv:hep-ph/0006239.

[36] T. Hirano, Phys. Rev. **C65** (2002) 011901, arXiv:nucl-th/0108004.

[37] C. Nonaka, S. A. Bass, Phys. Rev. **C75** (2007) 014902, arXiv:nucl-th/0607018.

[38] B. Schenke, S. Jeon, C. Gale, Phys. Rev. **C82** (2010) 014903, arXiv:1004.1408 [hep-ph].

[39] I. G. Bearden *et al.* (BRAHMS Collaboration), Phys. Rev. Lett. **94** (2005) 162301, arXiv:nucl-ex/0403050.

[40] J. P. Boris and D. L. Book, J. Comput. Phys. **A11** (1973) 38.

[41] S. T. Zalesak, J. Comput. Phys. **A31** (1979) 248.

[42] H. Niemi, PhD Thesis, "Hydrodynamical Flow and Hadron Spectra in Ultrarelativistic Heavy Ion Collisions at RHIC and the LHC", Research Report 7/2008, University of Jyväskylä, Finland.

[43] J. Sollfrank, P. Huovinen, M. Kataja, P. V. Ruuskanen, M. Prakash, R. Venugopalan, Phys. Rev. **C55** (1997) 392-410, arXiv:nucl-th/9607029.

[44] M. Laine, Y. Schroder, Phys. Rev. **D73** (2006) 085009, arXiv:hep-ph/0603048.

[45] F. Cooper, G. Frye, Phys. Rev. **D10** (1974) 186.

[46] K. J. Eskola, H. Niemi, P. V. Ruuskanen, Phys. Rev. **C77** (2008) 044907, arXiv:0710.4476 [hep-ph].

[47] D. Teaney, J. Lauret, E. V. Shuryak, Phys. Rev. Lett. **86** (2001) 4783-4786, arXiv:nucl-th/0011058.

[48] D. Teaney, J. Lauret, E. V. Shuryak, arXiv:nucl-th/0110037.

[49] T. Hirano, U. W. Heinz, D. Kharzeev, R. Lacey, Y. Nara, Phys. Lett. **B636** (2006) 299-304, arXiv:nucl-th/0511046.

[50] H. Petersen, J. Steinheimer, G. Burau, M. Bleicher, H. Stocker, Phys. Rev. **C78** (2008) 044901, arXiv:0806.1695 [nucl-th].

[51] H. Song, S. A. Bass, U. Heinz, Phys. Rev. **C83** (2011) 024912, arXiv:1012.0555 [nucl-th].

[52] H. Song, S. A. Bass, U. W. Heinz, T. Hirano, C. Shen, Phys. Rev. **C83** (2011) 054910, arXiv:1101.4638 [nucl-th].

[53] H. Song, S. A. Bass, U. W. Heinz, Phys. Rev. **C83** (2011) 054912, arXiv:1103.2380 [nucl-th].

[54] A. Muronga, D. H. Rischke, arXiv:nucl-th/0407114.

[55] M. Abramowitz, I. A. Stegun, "Handbook of Mathematical Functions with Formulas, Graphs, and Mathematical Tables", Dover, New York, 1964.

[56] M. Gyulassy, D. H. Rischke, B. Zhang, Nucl. Phys. **A613** (1997) 397-434, arXiv:nucl-th/9609030.

[57] R. Andrade, F. Grassi, Y. Hama, T. Kodama, O. Socolowski, Jr., Phys. Rev. Lett. **97** (2006) 202302, arXiv:nucl-th/0608067.

[58] R. P. G. Andrade, F. Grassi, Y. Hama, T. Kodama, W. L. Qian, Phys. Rev. Lett. **101** (2008) 112301, arXiv:0805.0018 [hep-ph].

[59] H. Petersen, M. Bleicher, Phys. Rev. **C79** (2009) 054904, arXiv:0901.3821 [nucl-th].

[60] K. Werner, I. Karpenko, T. Pierog, M. Bleicher, K. Mikhailov, Phys. Rev. **C82** (2010) 044904, arXiv:1004.0805 [nucl-th].

[61] H. Petersen, G.-Y. Qin, S. A. Bass, B. Muller, Phys. Rev. **C82** (2010) 041901, arXiv:1008.0625 [nucl-th].

[62] G.-Y. Qin, H. Petersen, S. A. Bass, B. Muller, Phys. Rev. **C82** (2010) 064903, arXiv:1009.1847 [nucl-th].

[63] B. Schenke, S. Jeon, C. Gale, Phys. Rev. Lett. **106** (2011) 042301, arXiv:1009.3244 [hep-ph].

[64] B. Schenke, S. Jeon, C. Gale, Phys. Lett. **B702** (2011) 59-63, arXiv:1102.0575 [hep-ph].

[65] Z. Qiu, U. W. Heinz, arXiv:1104.0650 [nucl-th].

[66] H. Petersen, arXiv:1105.1766 [nucl-th].

[67] K. J. Eskola, H. Niemi, P. V. Ruuskanen, S. S. Räsänen, Phys. Lett. **B566** (2003) 187-192, arXiv:hep-ph/0206230.

[68] J. Sollfrank, P. Koch, U. W. Heinz, Z. Phys. **C52** (1991) 593-610.

[69] S. S. Räsänen, MSc Thesis, University of Jyväskylä, 2001.

[70] T. Sjostrand, S. Mrenna, P. Z. Skands, JHEP **0605** (2006) 026, arXiv:hep-ph/0603175.

[71] C. Eckart, Phys. Rev. **58** (1940) 919-924.

[72] P. Romatschke, Int. J. Mod. Phys. **E19** (2010) 1-53, arXiv:0902.3663 [hep-ph].

[73] W. Israel, Annals Phys. **100** (1976) 310-331.

[74] W. Israel, J. M. Stewart, Annals Phys. **118** (1979) 341-372.

[75] A. Muronga, Phys. Rev. Lett. **88** (2002) 062302, arXiv:nucl-th/0104064.

[76] A. Muronga, Phys. Rev. **C69** (2004) 034903, arXiv:nucl-th/0309055.

[77] R. Baier, P. Romatschke, Eur. Phys. J. **C51** (2007) 677-687, arXiv:nucl-th/0610108.

[78] P. Romatschke, Eur. Phys. J. **C52** (2007) 203-209, arXiv:nucl-th/0701032.

[79] M. Luzum, P. Romatschke, Phys. Rev. Lett. **103** (2009) 262302, arXiv:0901.4588 [nucl-th].

[80] H. Song, U. W. Heinz, Phys. Lett. **B658** (2008) 279-283, arXiv:0709.0742 [nucl-th].

[81] H. Song, U. W. Heinz, Phys. Rev. **C77** (2008) 064901, arXiv:0712.3715 [nucl-th].

[82] C. Shen, U. Heinz, P. Huovinen, H. Song, Phys. Rev. **C82** (2010) 054904, arXiv:1010.1856 [nucl-th].

[83] H. Niemi, G. S. Denicol, P. Huovinen, E. Molnar, D. H. Rischke, Phys. Rev. Lett. **106** (2011) 212302, arXiv:1101.2442 [nucl-th].

[84] K. Dusling, D. Teaney, Phys. Rev. **C77** (2008) 034905, arXiv:0710.5932 [nucl-th].

[85] H. Song, U. W. Heinz, Phys. Rev. **C81** (2010) 024905, arXiv:0909.1549 [nucl-th].

[86] A. Monnai, T. Hirano, Phys. Rev. **C80** (2009) 054906, arXiv:0903.4436 [nucl-th].

[87] K. Dusling, G. D. Moore, D. Teaney, Phys. Rev. **C81** (2010) 034907, arXiv:0909.0754 [nucl-th].

[88] M. Luzum, J.-Y. Ollitrault, Phys. Rev. **C82** (2010) 014906, arXiv:1004.2023 [nucl-th].

[89] M. L. Miller, K. Reygers, S. J. Sanders, P. Steinberg, Ann. Rev. Nucl. Part. Sci. **57** (2007) 205-243, arXiv:nucl-ex/0701025.

[90] D. G. d'Enterria, D. Peressounko, Eur. Phys. J. **C46** (2006) 451-464, arXiv:nucl-th/0503054.

[91] S. S. Räsänen, Nucl. Phys. **A715** (2003) 717-725, arXiv:nucl-th/0210007.

[92] R. Chatterjee, E. S. Frodermann, U. W. Heinz, D. K. Srivastava, Phys. Rev. Lett. **96** (2006) 202302, arXiv:nucl-th/0511079.

[93] P. F. Kolb, U. W. Heinz, P. Huovinen, K. J. Eskola, K. Tuominen, Nucl. Phys. **A696** (2001) 197-215, arXiv:hep-ph/0103234.

[94] P. Huovinen, Nucl. Phys. **A761** (2005) 296-312, arXiv:nucl-th/0505036.

[95] M. Alvioli, H.-J. Drescher, M. Strikman, Phys. Lett. **B680** (2009) 225-230, arXiv:0905.2670 [nucl-th].

[96] M. Alvioli, K. J. Eskola, H. Holopainen, M. Strikman, *in progress*.

[97] W. Broniowski, M. Rybczynski, Phys. Rev. **C81** (2010) 064909, arXiv:1003.1088 [nucl-th].

[98] B. Alver, B. B. Back, M. D. Baker, M. Ballintijn, D. S. Barton, R. R. Betts, R. Bindel, W. Busza *et al.*, Phys. Rev. **C77** (2008) 014906, arXiv:0711.3724 [nucl-ex].

[99] K. J. Eskola, P. V. Ruuskanen, S. S. Räsänen, K. Tuominen, Nucl. Phys. **A696** (2001) 715-728, arXiv:hep-ph/0104010.

[100] K. J. Eskola, H. Honkanen, H. Niemi, P. V. Ruuskanen, S. S. Räsänen, Phys. Rev. **C72** (2005) 044904, arXiv:hep-ph/0506049.

[101] K. J. Eskola, K. Tuominen, Phys. Rev. **D63** (2001) 114006, arXiv:hep-ph/0010319.

[102] H. Niemi, K. J. Eskola, P. V. Ruuskanen, Phys. Rev. **C79** (2009) 024903, arXiv:0806.1116 [hep-ph].

[103] J.-Y. Ollitrault, Phys. Rev. **D46** (1992) 229-245.

[104] B. Alver, G. Roland, Phys. Rev. **C81** (2010) 054905, arXiv:1003.0194 [nucl-th].

[105] J. Jia (for the ATLAS Collaboration), *Quark Matter 2011 proceedings*, arXiv:1107.1468 [nucl-ex].

[106] B. H. Alver, C. Gombeaud, M. Luzum, J.-Y. Ollitrault, Phys. Rev. **C82** (2010) 034913, arXiv:1007.5469 [nucl-th].

[107] A. M. Poskanzer, S. A. Voloshin, Phys. Rev. **C58** (1998) 1671-1678, arXiv:nucl-ex/9805001.

[108] N. Borghini, P. M. Dinh, J.-Y. Ollitrault, Phys. Rev. **C63** (2001) 054906, arXiv:nucl-th/0007063.

[109] N. Borghini, P. M. Dinh, J.-Y. Ollitrault, Phys. Rev. **C64** (2001) 054901, arXiv:nucl-th/0105040.

[110] A. Bilandzic, R. Snellings, S. Voloshin, Phys. Rev. **C83** (2011) 044913, arXiv:1010.0233 [nucl-ex].

[111] R. S. Bhalerao, N. Borghini, J.-Y. Ollitrault, Nucl. Phys. **A727** (2003) 373-426, arXiv:nucl-th/0310016.

[112] A. Bilandzic, N. van der Kolk, J.-Y. Ollitrault, R. Snellings, Phys. Rev. **C83** (2011) 014909, arXiv:0801.3915 [nucl-ex].

[113] J.-Y. Ollitrault, A. M. Poskanzer, S. A. Voloshin, Phys. Rev. **C80** (2009) 014904, arXiv:0904.2315 [nucl-ex].

[114] M. Luzum, J.-Y. Ollitrault, Phys. Rev. Lett. **106** (2011) 102301, arXiv:1011.6361 [nucl-ex].

[115] F. G. Gardim, F. Grassi, Y. Hama, M. Luzum, J.-Y. Ollitrault, Phys. Rev. **C83** (2011) 064901, arXiv:1103.4605 [nucl-th].

[116] J.-Y. Ollitrault, Phys. Rev. **D48** (1993) 1132-1139, arXiv:hep-ph/9303247.

[117] S. Voloshin, Y. Zhang, Z. Phys. **C70** (1996) 665-672, arXiv:hep-ph/9407282.

[118] R. Chatterjee, D. K. Srivastava, Phys. Rev. **C79** (2009) 021901, arXiv:0809.0548 [nucl-th].

[119] F.-M. Liu, T. Hirano, K. Werner, Y. Zhu, Phys. Rev. **C80** (2009) 034905, arXiv:0902.1303 [hep-ph].

[120] P. B. Arnold, G. D. Moore, L. G. Yaffe, JHEP **0111** (2001) 057, arXiv:hep-ph/0109064.

[121] P. B. Arnold, G. D. Moore, L. G. Yaffe, JHEP **0112** (2001) 009, arXiv:hep-ph/0111107.

[122] F. Karsch, Z. Phys. **C38** (1988) 147.

[123] J. I. Kapusta, P. Lichard, and D. Seibert, Phys. Rev. **D44** (1991) 2774.

[124] L. Xiong, E. V. Shuryak, G. E. Brown, Phys. Rev. **D46** (1992) 3798-3801, arXiv:hep-ph/9208206.

[125] H. Nadeau, J. I. Kapusta, and P. Lichard, Phys. Rev. **C45** (1992) 3034.

[126] S. Turbide, R. Rapp, C. Gale, Phys. Rev. **C69** (2004) 014903, arXiv:hep-ph/0308085.

[127] P. Aurenche, M. Fontannaz, J.-P. Guillet, E. Pilon, M. Werlen, Phys. Rev. **D73** (2006) 094007, arXiv:hep-ph/0602133.

[128] F. Arleo, K. J. Eskola, H. Paukkunen, C. A. Salgado, JHEP **1104** (2011) 055, arXiv:1103.1471 [hep-ph].

[129] K. J. Eskola, H. Paukkunen, C. A. Salgado, JHEP **0904** (2009) 065, arXiv:0902.4154 [hep-ph].

[130] S. Turbide, C. Gale, E. Frodermann, U. Heinz, Phys. Rev. **C77** (2008) 024909, arXiv:0712.0732 [hep-ph].

[131] R. J. Fries, B. Muller, D. K. Srivastava, Phys. Rev. Lett. **90** (2003) 132301, arXiv:nucl-th/0208001.

[132] R. J. Fries, B. Muller, D. K. Srivastava, Phys. Rev. **C72** (2005) 041902, arXiv:nucl-th/0507018.

[133] F.-M. Liu, T. Hirano, K. Werner, Y. Zhu, Phys. Rev. **C79** (2009) 014905, arXiv:0807.4771 [hep-ph].

[134] G.-Y. Qin, J. Ruppert, C. Gale, S. Jeon, G. D. Moore, Phys. Rev. **C80** (2009) 054909, arXiv:0906.3280 [hep-ph].

[135] A. Adare *et al.* (PHENIX Collaboration), arXiv:1105.4126 [nucl-ex].

[136] R. Chatterjee, H. Holopainen, T. Renk, K. J. Eskola, *in progress.*

[137] S. S. Adler *et al.* (PHENIX Collaboration), Phys. Rev. Lett. **98** (2007) 012002, arXiv:hep-ex/0609031.

[138] S. S. Adler *et al.* (PHENIX Collaboration), Phys. Rev. Lett. **94** (2005) 232301, arXiv:nucl-ex/0503003.

[139] A. Adare *et al.* (PHENIX Collaboration), Phys. Rev. Lett. **104** (2010) 132301, arXiv:0804.4168 [nucl-ex].

[140] K. Aamodt *et al.* (ALICE Collaboration), Phys. Lett. **B696** (2011) 30-39, arXiv:1012.1004 [nucl-ex].

[141] H. Appelshaeuser (for the ALICE Collaboration), *Quark Matter 2011 proceedings.*

[142] R. Baier, Y. L. Dokshitzer, A. H. Mueller, S. Peigne, D. Schiff, Nucl. Phys. **B484** (1997) 265-282, arXiv:hep-ph/9608322.

[143] C. A. Salgado, U. A. Wiedemann, Phys. Rev. **D68** (2003) 014008, arXiv:hep-ph/0302184.

[144] X.-N. Wang, X. Guo, Nucl. Phys. **A696** (2001) 788-832, arXiv:hep-ph/0102230.

[145] S. Jeon, G. D. Moore, Phys. Rev. **C71** (2005) 034901, arXiv:hep-ph/0309332.

[146] M. Gyulassy, P. Levai, I. Vitev, Nucl. Phys. **B571** (2000) 197-233, arXiv:hep-ph/9907461.

[147] T. Renk, Phys. Rev. **C78** (2008) 034908, arXiv:0806.0305 [hep-ph].

[148] T. Renk, Phys. Rev. **C79** (2009) 054906, arXiv:0901.2818 [hep-ph].

[149] K. Zapp, G. Ingelman, J. Rathsman, J. Stachel, U. A. Wiedemann, Eur. Phys. J. **C60** (2009) 617-632, arXiv:0804.3568 [hep-ph].

[150] B. Schenke, C. Gale, S. Jeon, Phys. Rev. **C80** (2009) 054913, arXiv:0909.2037 [hep-ph].

[151] J. Auvinen, K. J. Eskola, T. Renk, Phys. Rev. **C82** (2010) 024906, arXiv:0912.2265 [hep-ph].

[152] S. A. Bass, C. Gale, A. Majumder, C. Nonaka, G.-Y. Qin, T. Renk, J. Ruppert, Phys. Rev. **C79** (2009) 024901, arXiv:0808.0908 [nucl-th].

[153] S. Afanasiev *et al.* (PHENIX Collaboration), Phys. Rev. **C80** (2009) 054907, arXiv:0903.4886 [nucl-ex].

[154] J. Auvinen, K. J. Eskola, H. Holopainen, T. Renk, Phys. Rev. **C82** (2010) 051901, arXiv:1008.4657 [hep-ph].

[155] T. Renk, H. Holopainen, J. Auvinen, K. J. Eskola, submitted to Phys. Rev. **C**, arXiv:1105.2647 [hep-ph].

[156] S. S. Adler *et al.* (PHENIX Collaboration), Phys. Rev. **C69** (2004) 034909, arXiv:nucl-ex/0307022.

[157] S. Afanasiev *et al.* (PHENIX Collaboration), Phys. Rev. **C80** (2009) 024909, arXiv:0905.1070 [nucl-ex].

[158] A. Adare *et al.* (PHENIX Collaboration), Phys. Rev. Lett. **105** (2010) 062301, arXiv:1003.5586 [nucl-ex].

[159] J. Adams *et al.* (STAR Collaboration), Phys. Rev. **C72** (2005) 014904, arXiv:nucl-ex/0409033.

[160] A. Adare *et al.* (PHENIX Collaboration), arXiv:1105.3928 [nucl-ex].

[161] A. Adare *et al.* (PHENIX Collaboration), Phys. Rev. **C81** (2010) 034911, arXiv:0912.0244 [nucl-ex].

[162] K. Dusling, I. Zahed, Phys. Rev. **C82** (2010) 054909, arXiv:0911.2426 [nucl-th].

[163] R. Rapp, J. Wambach, Eur. Phys. J. **A6** (1999) 415-420, arXiv:hep-ph/9907502.

[164] H. Bebie, P. Gerber, J. L. Goity, H. Leutwyler, Nucl. Phys. **B378** (1992) 95-130.

[165] K. J. Eskola, H. Holopainen, R. Paatelainen, *in progress*.

[166] K. Aamodt *et al.* (ALICE Collaboration), Phys. Rev. Lett. **105** (2010) 252301, arXiv:1011.3916 [nucl-ex].

[167] B. B. Back *et al.* (PHOBOS Collaboration), Phys. Rev. **C72** (2005) 051901, arXiv:nucl-ex/0407012.

[168] M. Dion, C. Gale, S. Jeon, J. -F. Paquet, B. Schenke, C. Young, *Quark Matter 2011 proceedings*, arXiv:1107.0889 [hep-ph].

[169] K. Dusling, Nucl. Phys. **A839** (2010) 70-77, arXiv:0903.1764 [nucl-th].

[170] B. Mohanty, *Quark Matter 2011 proceedings*, arXiv:1106.5902 [nucl-ex].